

1
2
3
4
5
6
7
8
9
10
11
12
13
14
15
16
17
18
19
20
21
22
23
24
25
26
27
28
29
30
31
32
33
34
35
36
37
38
39
40
41
42
43
44
45
46

Evaluation of Precipitation from EURO-CORDEX Regional Climate Simulations in a Small-Scale Mediterranean Site

Giuseppe Mascaro¹, Francesco Viola², and Roberto Deidda²

¹ School of Sustainable Engineering and the Built Environment, Arizona State University, Tempe, AZ, USA

² Dipartimento di Ingegneria Civile, Ambientale ed Architettura Università degli Studi di Cagliari, Cagliari, Italy.

An edited version of this paper was published by AGU. Copyright (2018) American Geophysical Union (+)

Mascaro, G., Viola, F., & Deidda, R. (2018). Evaluation of precipitation from EURO-CORDEX regional climate simulations in a small-scale Mediterranean site. *Journal of Geophysical Research: Atmospheres*, 123. <https://doi.org/10.1002/2017JD027463>

Corresponding Author: Giuseppe Mascaro, College Avenue Commons (CAVC), 660 S. College Avenue, #507, Tempe, AZ 85281. Email: gmascaro@asu.edu

47 **Abstract**

48

49 The evaluation of regional climate models' (RCMs) ability to reproduce the present-day climate
50 is critical to support their utility in impact studies under future climatic scenarios. This study evaluates
51 the skill of an ensemble of state-of-the-art regional climate simulations from the EURO-CORDEX
52 initiative in reproducing the precipitation (P) properties in Sardinia, a Mediterranean island of ~24,000
53 km². The ensemble includes simulations at 0.44° and 0.11° grid resolution of the "Historical"
54 experiment from 1950 to 2005. Precipitation records from a high-density network of gauges are used as
55 reference dataset. The interannual and seasonal climatology of P, presence of trend, and orographic
56 effect are assessed at the original RCM resolutions and different spatial scales of aggregation. Most
57 models capture the observed positive relation between annual P and elevation, with better performance
58 at 0.11° resolution. The simulated spatial patterns of the climatological annual and seasonal means are
59 well correlated with the observation at both resolutions, but their spatial variability is overestimated.
60 Positive and negative bias of up to ±60% are found in the simulation of annual mean and interannual
61 variability. While the majority of the models reproduce the phase of the seasonal cycle, they
62 underestimate (overestimate) winter (summer) P. The RCMs exhibit different deficiencies in capturing
63 the negative annual and seasonal observed trends. In general, models' skill degrades when analyses are
64 conducted at smaller aggregation scales. Results of this study reveal insight on RCM performances in
65 small-scale regions, which are often targeted by impact studies and have so far received less attention.

66

67 **1. Introduction**

68
69 Dynamical downscaling is a technique aimed at increasing the resolution of General Circulation
70 Models (GCMs) by nesting Regional Climate Models (RCMs) into GCM outputs over targeted
71 domains (Giorgi & Mearns, 1999). In such a way, while GCMs are able to represent large-scale
72 forcings (e.g., monsoons, El Niño Southern Oscillation, North Atlantic Oscillation), RCMs run at
73 higher resolution have the potential to capture the impact on climate due to local forcings, such as
74 complex topography, heterogeneity in land cover, and coastlines (Giorgi & Gutowski Jr, 2015). Since
75 the idea of dynamical downscaling was originated in the late 1980s, several RCMs have been
76 developed, improved, and applied throughout the world to produce high-resolution climate information
77 under potential future scenarios for a range of impacts studies, including hydrologic analyses (Piras et
78 al., 2014, 2016; Senatore et al., 2011; Sulis et al., 2011, 2012; Trambly et al., 2013; Viola et al., 2016),
79 quantification of agricultural productivity (Bird et al., 2016; Soddu et al., 2013; Viola et al., 2014;
80 Voloudakis et al., 2015), and evaluation of infrastructure performance and failures (Bhatkoti et al.,
81 2016; Kuo & Gan, 2015) among others.

82 The Coordinated Regional Downscaling Experiment (CORDEX) is the first international
83 program that has been designed to offer a common framework for conducting regional climate
84 simulations in a set of domains that cover all land areas of the Earth. In CORDEX, GCMs from the
85 Coupled Model Intercomparison Project phase 5 (CMIP5) (Taylor et al., 2012) are used to force an
86 ensemble of RCMs. The CORDEX experiments have the goal of simulating both historical and future
87 climate under different Representative Concentration Pathways (Van Vuuren et al., 2011). Three sets of
88 experiments were performed in CORDEX: 1) “Historical”, where RCMs are driven by GCMs used in
89 CMIP5 to reproduce the 1950–2005 climate; 2) “Evaluation”, where RCMs are forced by the European
90 Centre for Medium-Range Weather Forecasts Interim Re-Analysis (ERA- Interim; (Dee et al., 2011))
91 in the period 1989-2008; and 3) “Scenarios”, where RCMs are driven by GCMs from CMIP5 under

92 different RCP scenarios of the future climate from 2006 to 2100. The multimodal ensemble of regional
93 climate projections of CORDEX offers a unique opportunity to assess and compare performance of
94 GCM-RCM combinations, explore the different sources of uncertainty, and identify deficiencies of
95 GCMs, RCMs and their combinations.

96 One of the CORDEX domains is centered on the European continent and is known as EURO-
97 CORDEX (Jacob et al., 2014). This includes the Mediterranean region, which many studies predict to
98 be one of the hot spots of climate change owed to a future increase in temperature and decrease in
99 precipitation (Giorgi, 2006; Kjellström et al., 2013). Despite this overall tendency, the sign and
100 magnitude of the changes in temperature and precipitation vary in space depending on the future
101 climate scenario, type and resolution of climate models, as well as on the configuration of climate
102 experiments (Giorgi & Lionello, 2008; Ozturk et al., 2015). This uncertainty is due, in part, to the
103 spatial heterogeneity of climatic features in the Mediterranean region (Lionello et al., 2006) that are
104 difficult to capture. Specifically, precipitation is characterized by (i) high spatial variability, which is
105 partially controlled by orography (Ehmele et al., 2015; Godart et al., 2011); (ii) strong seasonality; (iii)
106 large inter-annual fluctuations; and (iv) occurrence of extremes, including periods of prolonged
107 droughts (Cook et al., 2016) and high-intensity storms leading to devastating floods and flash floods
108 (Chessa et al., 2004; Gascón et al., 2016; Silvestro et al., 2012; Tarolli et al., 2012). Furthermore,
109 recent studies have presented evidence of decreasing trends in observed annual precipitation in the
110 eastern (Amanatidis et al., 1993; Kutiel et al., 1996; Türkeş, 1996), central (Cannarozzo et al., 2006;
111 Piervitali et al., 1998) and western (Alpert et al., 2002; De Luís et al., 2000; Esteban-Parra et al., 1998;
112 Gonzalez-Hidalgo et al., 2009; Lázaro et al., 2001) parts of the Mediterranean region, which in most
113 cases were found to be caused by a reduction of P in winter (Cannarozzo et al., 2006; Norrant &
114 Douguédroit, 2006; Trigo et al., 2000).

115 In addition to CORDEX, prior research initiatives have provided access to outputs of RCMs
116 forced by GCMs, including PRUDENCE (Christensen et al., 2007) and ENSEMBLES (van der Linden
117 & Mitchell, 2009) experiments. Performances of RCMs available through these open data projects
118 have been evaluated during the historical period, focusing in most cases on large macroregions
119 characterized by relatively homogeneous climatic features. In the Mediterranean region, Jacob et al.
120 (2007) found that the PRUDENCE RCMs exhibit negative (positive) bias in the prediction of winter
121 (summer) precipitation (P) and temperature (T). Kotlarski et al. (2014) analyzed the performance of an
122 ensemble of 17 RCMs of EURO-CORDEX in the Evaluation experiment and found that most RCMs:
123 (i) have a positive (negative) bias in the prediction of seasonal and annual P (T); (ii) significantly
124 overestimate (reproduce fairly well) the spatial variability of P (T); (iii) overestimate the interannual
125 variability of P and T; and (iv) do not exhibit clear improvements when the grid resolution is increased
126 from 0.44° to 0.11°. A limited number of studies has instead investigated performance of climate
127 simulations at smaller scales, where climate change is expected to impact natural resources and local
128 economies (e.g., Ludwig and Roson (2016) and references therein). For example, Deidda et al. (2013)
129 compared the skill of 14 GCM-RCM combinations at 0.22° grid spacing from the ENSEMBLES
130 project in six Mediterranean catchments of areas ranging from ~250 to ~3500 km² spanning different
131 climatic regimes, using daily gridded E-OBS dataset at 0.25° resolution as reference (Haylock et al.,
132 2008). Their analysis revealed that most models (i) overestimate P, especially in summer and in basins
133 where summer months are extremely dry; and (ii) capture the seasonality of T, with biases often larger
134 than 5 K.

135 In this study, we complement and expand previous intercomparison analyses by evaluating the
136 performance of several state-of-the-art regional climate simulations of the Historical experiment of
137 EURO-CORDEX at 0.44° (~50 km) and 0.11° (~12 km) grid resolution in reproducing the precipitation
138 annual and seasonal regimes and trends in the island of Sardinia, Italy. While the majority of prior

139 work examined medium-to-large regions or basins of the world (Jacob et al., 2007; Kotlarski et al.,
140 2014; Lorenz & Jacob, 2010; Lucarini et al., 2007; Mascaro et al., 2015; Nikulin et al., 2012), we focus
141 on a relatively small domain (~24,000 km²) with complex topography where the added value of RCMs
142 is expected to be high (e.g., Torma et al., 2015). This is important to increase the utility of regional
143 climate simulations in vulnerability, impact, and adaptation studies at local scales. Different from
144 previous analyses that adopted gridded observational products at relatively coarse resolution, often
145 derived from low-density sparse networks of rain gauges (Hanel & Buishand, 2011), we use long-term
146 P records from a network of more than 400 gauges (more than one gauge per 100 km²), thus
147 minimizing the observational uncertainty (Prein & Gobiet, 2017). As done in previous studies, we
148 evaluate the ability of coupled GCM and RCMs in reproducing interannual and seasonal variability of
149 P. In addition, taking advantage of the high-density observational dataset, we investigate two factors
150 that so far have received less attention, including the simulation of orographic effects and of historical
151 trends. Specifically, we first compare the ability of each GCM-RCM combination to capture the link
152 between annual P and elevation. Next, we investigate the spatial patterns of climatological annual and
153 seasonal mean P. These analyses are conducted on model outputs at their original grid resolutions of
154 0.44° and 0.11°. Subsequently, we carry out a set of analyses on model outputs and observations
155 aggregated at multiple scales, ranging from the entire island (~24,000 km²) to ~6,000 km², with the
156 goal of evaluating how the spatial scale of aggregation affects model performances in reproducing the
157 annual and seasonal P climatology, as well as the observed trends. Given the availability of an
158 ensemble of GCM-RCM combinations, we also assess whether the nested RCM or driving GCM exert
159 a dominant control on the simulation of the analyzed precipitation climatological properties. Finally,
160 we provide guidance on the performances of each GCM-RCM combination in reproducing different P
161 properties, with the aim of supporting future impact studies in the region.

162

163 2. Study Area and Datasets

164

165 The study area is Sardinia (Italy), a Mediterranean island of $\sim 24,000 \text{ km}^2$ located about 400 km
166 west off of the Italian peninsula (Fig. 1a). As shown in the digital elevation model (DEM) reported in
167 Fig. 1b, Sardinia is characterized by complex topography with the presence of a long mountain range,
168 called the Sardinian–Corse Mountain System, which runs from south to north in the eastern part of the
169 island. In addition, a smaller isolated mountain range is located in the southwest. The climate is
170 typically Mediterranean, with the occurrence of a wet period from September to May and very dry
171 summers from June to August. As reported by Chessa et al. (1999) and Mascaro et al. (2013), during
172 the wet period three main weather regimes tend to occur, which are caused by different synoptic
173 patterns and are affected by local terrain properties. The first two lead to P distributions with
174 decreasing intensity from southwest to northeast and from northwest to southwest, respectively. In both
175 cases, large frontal systems transported by northwesterly flows (the mistral wind) cause widespread
176 precipitation in the island, with lower amounts in the eastern part due to the Sardinian–Corse Mountain
177 System that acts as a barrier. In contrast, the third weather regime is associated with southeasterly
178 winds (the sirocco wind) advecting moist air at lower levels of the atmosphere, while, at the same time,
179 cold air is transported from the north at upper levels. These conditions, combined with the orographic
180 barriers, lead to high-intensity storms (including some extreme events exceeding 500 mm in 24 h) in
181 the windward side of the island. Overall, the spatial distribution of P in the third regime is characterized
182 by a strong east–west negative gradient.

183 The observational dataset used in this study includes daily P data collected by the network of
184 441 rain gauges of the Sardinian Hydrological Survey, of which 229 (256) have more than 50 (30)
185 years of observations. As shown in Fig. 1b, the gauges are distributed quite uniformly throughout the
186 island (at least one gauge per 100 km^2) and cover a wide range of elevation. Table 1 summarizes the
187 basic statistics of gauge elevation, and annual and seasonal P recorded over the period 1950–2005. The

188 mean annual P is 710 mm with lower values (316 mm) in a wide plain area in the southeastern part, and
189 larger amounts (up to 1281 mm) in the highest mountains. The pluviometric regime is characterized by
190 a strong seasonality, with most of the annual P (68%) falling from September to February. The seasonal
191 P is also affected by large spatial variability. For instance, the mean recorded value in winter (DJF) is
192 260 mm, with a minimum of 69 mm and a maximum of 495 mm, again following the elevation
193 gradient. The mean summer (JJA) rainfall is instead about 43 mm, ranging from 9 mm to 202 mm.

194 Climate model outputs were obtained from EURO-CORDEX at the spatial resolutions of 0.44°
195 and 0.11° (hereafter EUR-44 and EUR-11, respectively). The EURO-CORDEX domain is shown in
196 Fig. 1a, while the grid centers of the RCMs of EUR-44 and EUR-11 in Sardinia are reported with black
197 circles in Figs. 1c,d, respectively. Model outputs of daily P were acquired for the Historical
198 experiment: the lists of GCMs and RCMs used in this study, including a description of the short names,
199 are presented in Tables 2 and 3, respectively. The GCM-RCM combinations for EUR-44 and EUR-11
200 are instead listed in Table 4. For EUR-44 (EUR-11), a total of 18 (15) GCM-RCM combinations were
201 available, which include 10 (5) GCMs and 7 (6) RCMs. For both grid resolutions: (i) RCA4 was driven
202 by all the GCMs used in each case; and (ii) two realizations generated under different initial conditions
203 were available for the combination MPI-ESM-LR-REMO2009. For EUR-44 (EUR-11), the number of
204 RCMs downscaling the same GCM ranges from 1 to 3 (1 to 4). The terrain elevation grid of each RCM
205 was also collected to evaluate the orographic effect on precipitation. Results presented in this study
206 were in general produced using all available GCM-RCM combinations in Table 4. However, some
207 analyses aimed at investigating the importance of the RCM resolution were conducted on a subset of
208 eleven GCM-RCM combinations where both EUR-44 and EUR-11 runs were available (highlighted
209 entries in Table 4).

210

211

212 **3. Methods**

213

214 **3.1 Data Preprocessing**

215 Climate model outputs and gauge observations were interpolated on non-rotated regular grids at
216 resolutions commensurate to the EUR-44 and EUR-11 rotated grids. For EUR-44, the resolution of 0.5°
217 (~50 km) was selected, while, for EUR-11, a spacing of 0.1° (~10 km) was chosen. This allowed
218 conducting analyses in common spatial references. Figs. 1c-d show the two original rotated grids along
219 with the regular grids used for the interpolation. A strategy mimicking the Thiessen polygon approach
220 was adopted to resample both model outputs and the gauge records. First, a high-resolution (0.01°; ~1
221 km) grid covering the island was defined. The P value in each pixel of the high-resolution grid was
222 assumed equal to the value simulated (observed) in the nearest model grid point (rain gauge). The
223 resulting P field was then resampled at 0.1° and 0.5° resolution by averaging the values in the pixels at
224 0.01° resolution. The same approach was also used to resample the elevation grids of the RCMs. For
225 simplicity, in the following: (i) the labels EUR-44 and EUR-11 will be used to refer also to the
226 corresponding interpolated grids; and (ii) the words “resolution” and “spacing” will be used
227 interchangeably to refer to the horizontal grid spacing of the models.

228 In addition to analyses at the non-rotated regular grids described above, we also investigated the
229 models’ ability to simulate the climatology of P at different spatial scales. For this aim, the daily grids
230 were aggregated at different spatial scales: (i) over the entire island (labeled as “Full” scale in the
231 following); (ii) over the eastern (E) and western (W) halves (“Half” scale); and (iii) over the
232 southeastern (SE), southwestern (SW), northeastern (NE), and northwestern (NW) quarters (“Quarter”
233 scale). For the Half scale, the choice of dividing the island into E and W was motivated by the goal of
234 assessing whether the models are able to capture the main precipitation regimes that are characterized
235 by marked E-W gradients, as discussed in the previous section. Depending on the analyses, daily data
236 were aggregated also at different temporal scales, namely at annual, seasonal and monthly scales. The

237 same procedures were also applied to the observed data for the same period of the Historical
238 experiment from 1950 to 2005. All the land points were utilized in the analyses.

239 240 **3.2 Analyses at EUR-44 and EUR-11 Grid Resolutions**

241 The models' capability in capturing the observed orographic effect on precipitation was
242 investigated under the hypothesis that a linear dependence can explain the linkage between mean
243 annual P and elevation at each pixel of EUR-44 and EUR-11 interpolated grids. The analysis was
244 conducted using the proper terrain grid for each RCM, while a 10-m Digital Elevation Model, freely
245 available from the official website of the Sardinian Region, was utilized for the rain gauge
246 observations. The Taylor diagram (Taylor, 2001) was used to quantitatively compare the spatial
247 patterns of climatological mean annual, and winter (DJF) and summer (JJA) seasonal P simulated by
248 the models and observed at both EUR-44 and EUR-11 resolutions across the available 56 years. The
249 Taylor diagram shows in the same space three metrics, including coefficient of correlation (CC),
250 standard deviation, and centered root mean square error (RMSE), defined as the RMSE of the
251 anomalies (i.e., the variables of interest minus the corresponding mean). To compare different seasons
252 and grid resolutions where the observed values change, we used the normalized Taylor diagram, which
253 is obtained by dividing standard deviation and centered RMSE by the observed standard deviation.

254 255 **3.3 Analyses at Multiple Spatial Scales**

256 A set of analyses was conducted to assess the model skill in reproducing different precipitation
257 properties of the past climate at multiple spatial scales (Full, Half and Quarter), including interannual,
258 monthly and seasonal variability, as well as presence of trends. For a given scale, the ability to capture
259 the interannual variability of P was investigated by calculating the climatological mean and coefficient
260 of variation (CV) of the annual P. Moreover, to compare simulated and observed values, we also
261 computed the relative bias defined as $(X_{sim} - X_{obs})/X_{obs} \times 100 \%$, where X_{sim} and X_{obs} are the
262 simulated and observed values for a given variable, respectively. The model skill to reproduce the

263 seasonal variability of the precipitation regime was tested by (i) comparing the climatological monthly
 264 mean P through the Taylor diagram (Taylor, 2001), and (ii) calculating the bias of P accumulated in the
 265 four seasons (DJF, MMA, JJA, SON). In addition, the existence of trends at annual and season scales
 266 was investigated through the Mann-Kendall test (Kendall, 1962; Mann, 1945). This is a non-parametric
 267 test that allows identifying the presence of statistically significant trends without any assumption on the
 268 underlying distribution. The Mann-Kendall test was here applied to evaluate at 95% confidence level
 269 the null hypothesis that no trend exists in the population from which the data is drawn. The magnitude
 270 of trends was also evaluated through the slope of the linear regression between P and time.

271 3.4 Quantification of Uncertainty due to RCMs and GCMs

272 The relative contribution of RCMs and GCMs to the uncertainty in the simulation of different
 273 precipitation properties was quantified by estimating the percent of variance explained by nested
 274 RCMs, driving GCMs, and interactions between them. For this aim, we used one of the methods based
 275 on analysis of variance (ANOVA) proposed by Déqué et al. (2012). Let us assume that N RCMs have
 276 been nested in M GCMs, thus leading to $N \times M$ GCM-RCM combinations. If X_{ij} is a given variable
 277 (e.g., the mean annual P) simulated by the i -th RCM ($i = 1, \dots, N$) nested in the j -th GCM ($j = 1, \dots,$
 278 M), the total variance V can be decomposed as:

$$280 \quad V = R + G + RG \quad (1)$$

281 where:

$$282 \quad R = \frac{1}{N} \sum_{i=1}^N (\bar{X}_{RCM,i} - \bar{X})^2 \quad (2)$$

$$283 \quad G = \frac{1}{M} \sum_{j=1}^M (\bar{X}_{GCM,j} - \bar{X})^2 \quad (3)$$

$$284 \quad RG = \frac{1}{M} \sum_{j=1}^M \frac{1}{N} \sum_{i=1}^N (X_{i,j} - \bar{X}_{RCM,i} - \bar{X}_{GCM,j} + \bar{X})^2 \quad (4)$$

285 In the equations above, $\bar{X}_{RCM,i} = \frac{1}{M} \sum_{j=1}^M X_{i,j}$ is the mean of the simulations of the i -th RCM forced by

286 all M GCMs, $\bar{X}_{GCM,j} = \frac{1}{N} \sum_{i=1}^N X_{i,j}$ is the mean of all N RCMs driven by the j -th GCM, and \bar{X} is the
 287 mean of all X_{ij} . Since, as shown in Table 4, not all RCMs are coupled with all GCMs and viceversa,
 288 several missing values occur in the $M \times N$ matrices of $X_{i,j}$ variables for EUR-44 and EUR-11. The
 289 following formula proposed by Déqué et al. (2012) was then used to fill the missing instances:

$$290 \quad X_{i,j} = \bar{X}_{RCM,i} + \bar{X}_{GCM,j} - \bar{X}. \quad (5)$$

291 Déqué et al. (2012) tested also an alternative approach to fill the missing values based on weather
 292 regimes, but could not draw definitive conclusions on which is the best performing one. Given its
 293 simplicity, we preferred using the reconstruction method of equation (5), which was also successfully
 294 applied by Heinrich et al. (2014).

295 3.5 *Metric for Ranking Climate Model Performances*

296 The GCM-RCM combinations were ranked based on their performances in capturing different P
 297 properties, namely orographic effect, interannual variability, seasonality, and annual trend. Following
 298 Deidda et al. (2013), we computed, for each property, a single dimensionless error metric that
 299 combines multiple variables characterizing that property (e.g., mean annual P and CV for interannual
 300 variability, see also Table 5). The general definition of the metric, ϵ_j , calculated for the j -th GCM-RCM
 301 combination ($j = 1, \dots, N$) is:

$$302 \quad \epsilon_j = \sqrt{\sum_{k=1}^S \left(\frac{E_{k,j}}{\sum_{i=1}^N E_{k,i}} \right)^2} \quad (6)$$

304 where $E_{k,j}$ is the error between observed and simulated values of the variable k ($k = 1, \dots, S$). In
 305 equation (6), $E_{k,j}$ was divided by the sum of the errors of all models to obtain a dimensionless
 306 contribution for the error of variable k . The contributions for all S variables were then summed. Table 5
 307 lists the variables chosen for each P property and describes how the corresponding errors were
 308 calculated. The models were ranked based on the value of ϵ_j (the lower the rank, the better the model

309 performances). This calculation was performed at the Full, Half and Quarter aggregation scales for all
310 properties except for the orographic effect that was evaluated at the original grid resolution.

311 **4. Results**

312 313 **4.1 Orographic Effect on Annual Precipitation**

314 The relation between mean annual P and elevation for the GCM-RCM combinations of EUR-44
315 is reported in Fig. 2a. In this and following figures, the same color was used to indicate the driving
316 GCM and the same marker for the RCM, while the star symbol was utilized for the rain gauge
317 observations. To facilitate the comparison among models and observation, the slope of the linear
318 regression is reported in Fig. 2b, using vertical dashed lines to indicate the cases where the linear
319 relation is statistically significant at 95%. This figure indicates that the main control in describing the
320 dependence of P on elevation is played by the RCMs. For example, RCA4 outputs show similar slopes
321 of the linear regression regardless of the driving GCM, while different RCMs nested in the same GCM
322 may display very different slopes (see e.g. RCMs nested on CNRM-CM5). Rain gauge observations
323 indicate that P increases with elevation with a rate of 0.46 mm/m. The majority of the RCMs also
324 simulate a positive linear relation that is statistically significant. However, the slope varies across the
325 models: the ten simulations of RCA4 display the largest slope (on average, 1.92 mm/m) followed by
326 ALADIN53 and RACMO22E, whose values are very close to the observation. Three RCMs
327 (ALADIN52, CCLM4-8-17, and REMO2009) are instead characterized by a negative slope, but the
328 linear regression is never statistically significant.

329 The relation between mean annual P and elevation was also investigated at the finer grid
330 resolution of EUR-11, with results reported in Figs. 2c,d. For the sake of clarity, in Fig. 2c the large
331 number of grid points of EUR-11 have been grouped in 10 classes of approximately equal sample size
332 and the mean of both P and elevation in each class has been plotted. The slopes of the linear regression
333 shown in Fig. 2d have been instead computed using all points. Our findings show that running the

334 models at reduced horizontal spacing significantly improves their ability to correctly reproduce the
335 positive relation between annual rainfall and elevation. This is true for all models, except for
336 REMO2009 that still simulates a negative slope. It is worth noticing that, while the slopes are all
337 similar, the models are characterized by different degrees of bias (i.e., the intercept of the regression
338 lines varies), as it will be discussed with larger detail in the next sections.

339 340 **4.2 Spatial Patterns at EUR-44 and EUR-11 Resolutions**

341 The comparison between simulated and observed spatial patterns of mean annual, winter and
342 summer P at EUR-44 and EUR-11 resolutions is summarized in Fig. 3 through the normalized spatial
343 Taylor diagrams. Additionally, the spatial maps of the annual P observed and simulated by two models
344 with contrasting performances are reported, as reference, in Fig. S1 of the supplementary materials.
345 The following considerations can be made. (1) For both EUR-11 and EUR-44 resolutions,
346 performances at annual scale are mostly determined by those in winter, which is by far the wettest
347 season (compare panels a with c and b with d in Fig. 3). (2) At EUR-44 grid resolution, most models
348 have a high CC (>0.7), but they overestimate the spatial variability with standard deviations reaching
349 more than 6 times the observed values in summer. (3) At EUR-44 resolution, three simulations driven
350 by MPI-ESM-LR, including the two ensemble members of REMO2009 and that with CCLM4-8-17,
351 have instead negative CC and high and low standard deviations and centered RMSE, respectively, at
352 annual and winter scale. A negative CC is also found for CNRM-CM5-ALADIN52 in winter. (4)
353 Increasing the grid resolution to EUR-11 leads to lower CC values (CC~0.6) for most models and an
354 increase of CC for the GCM-RCM combinations discussed in point (3). The values of the normalized
355 RMSE and standard deviations decrease, suggesting an improvement of the model performances for
356 these metrics. (5) The best performing regional climate simulations in reproducing the spatial patterns
357 across all seasons and resolutions are those by RACMO22E forced by HadGEM2-ES and EC-EARTH.

358

359 4.3 *Interannual Variability at Multiple Spatial Scales*

360 As a next step, we explored how model performances at annual scale vary with the spatial scale
361 of aggregation. Fig. 4 reports the scatterplots between mean annual P and CV observed and simulated
362 by the climate models at EUR-44 and EUR-11 grid resolutions at the Full scale. For EUR-44 (Fig. 4a),
363 the GCM-RCM combinations cluster around the observed mean annual P, simulating a fairly large
364 range of values with bias varying from -43 to +43%. Most models underestimate the interannual
365 variability and the bias of CV ranges from -27% to +34%. A group of regional climate simulations
366 capture quite well both mean annual P and CV, including the two ensemble members of REMO2009
367 forced by MPI-ESM-LR, all RCMs driven by EC-EARTH, and RCA4 driven by NorESM1-M. The
368 visual inspection of Fig. 4b suggests that decreasing the spacing to EUR-11 leads to a reduction in the
369 spread of mean annual P and CV simulated by the models, and a general improvement as compared to
370 EUR-44. The scatterplots for the other aggregation scales are instead reported in Figs. S2 and S3 of the
371 supplementary materials. At Half scale, the climate models capture the change in observed mean
372 annual P from W to E (from 677 to 740 mm), while showing the same inter-model variability found at
373 the Full scale. This is also true for results at Quarter scale in NE and SE, with a general tendency to
374 underestimate CV. In contrast, in the two western portions, the models exhibit slightly diverse patterns
375 of inter-model differences, mainly underestimating (overestimating) the mean P (CV) in SW (NW).

376 To properly compare results of EUR-44 and EUR-11 and investigate how performances change
377 with the scale, we focused on the GCM-RCM combinations available at both resolutions (highlighted
378 instances in Table 4). Fig. 5 shows the relative bias of mean annual P and CV simulated by these
379 combinations at all aggregation scales, derived from EUR-44 and EUR-11 resolutions (note that, in this
380 and following figures comparing the GCM-RCM combinations available at both resolutions, only one
381 ensemble member of MPI-ESM-LR–REMO2009 is shown because results for the other member are
382 very similar). We first notice that, at both resolutions, most models have a relatively constant bias at

383 Full and Half scale, but the bias fluctuates with the location at Quarter scale where the observed values
384 also differ (see Figs. S2 and S3). As a result, model performances decrease at smaller aggregation
385 scales depending on the location. For example, Fig. 5a shows that the bias of mean annual P of MPI-
386 ESM-LR-REMO2009 at EUR-44 resolution is ~0% at Full scale and $\pm 10\%$ at Half scale. At Quarter
387 scale, the bias varies instead over a much larger range ($\pm \sim 40\%$), consistent with the poor performance
388 of this model in the simulation of the spatial patterns at the original grid resolutions reported in the
389 Taylor diagrams. Considering now results for the mean annual P of all models, reducing the horizontal
390 grid spacing of the RCMs (i.e. from EUR-44 to EUR-11) leads to either small changes (about $\pm 5\%$) or
391 improved simulation performances (bias reduction $> 10\%$), with seven models clustering right below
392 the horizontal line of 0% bias in Fig. 5c. A notable exception is CNRM-CM5-ALADIN53, whose bias
393 rises on average by 15% from EUR-44 to EUR-11. The adoption of a higher-resolution domain in the
394 RCMs leads to slightly improved accuracy in the representation of the interannual P variability (Figs.
395 5b,d), with a mean bias reduction of about 5%. Apart from SW and SE for the mean annual P and NW
396 for CV, the improvements due to increasing grid resolution occur at all scales and locations.

397 398 **4.4 Annual Cycle and Seasonal Variability at Multiple Spatial Scales**

399 The annual cycle of P aggregated at Full scale is plotted in Fig. 6, which shows the mean
400 monthly values for all GCM-RCM combinations and observations at both resolutions. The Taylor
401 diagrams comparing simulated and observed mean monthly P aggregated at the Full scale and the
402 seasonal bias are instead presented in Fig. 7. Most climate models reproduce fairly well the phase of
403 the seasonal cycle of P ($CC > 0.8$ in Figs. 7a,c), but with different accuracy (centered RMSE ranging
404 from 10 to 45 mm). Furthermore, almost all models underestimate the amplitude of the cycle, as
405 suggested by simulated standard deviations smaller than the observed value. Clustering of colors in Fig.
406 6 and in the Taylor diagrams of Fig. 7 clearly indicates that GCMs control the reproduction of the
407 annual cycle. The majority of the RCMs driven by CNRM-CM5 and HadGEM2-ES fail in simulating

408 the seasonality at both resolutions, as they are characterized by negative CC and centered RMSE > 30
409 mm. In contrast, the RCMs driven by MPI-ESM-LR exhibit the best performance metrics. The analysis
410 of the seasonal bias (Figs. 7c,d) provides insight about the reasons of model deficiencies and skills. At
411 both resolutions, most models: (i) underestimate P in DJF and SON with biases reaching -62%, (ii)
412 have positive or negative biases of about $\pm 50\%$ in MAM, and (iii) overestimate P in JJA, especially
413 those driven by CNRM-CM5, GFDL-ESM2M and HadGEM2-ES whose bias reaches values larger
414 than +300%. The biases are lower for the RCMs forced by MPI-ESM-LR and EC-EARTH.

415 To compare results of EUR-44 and EUR-11 and, at the same time, investigate the role of
416 aggregation scale and location, the standard deviation and centered RMSE of the GCM-RCM
417 combinations available at both resolutions (entries highlighted in Table 4) have been reported in Fig. 8
418 for the different scales. The observed spatial standard deviation has also been showed. The figures
419 suggest that, overall, increasing the RCM grid resolution does not have significant impacts on the
420 models' ability in reproducing the intra-annual variability of P and that, actually, performances of some
421 RCMs degrade at EUR-11 horizontal spacing. This result can be somewhat expected since the forcing
422 GCM appears to be the main control on this feature. The observed amplitude of the seasonal cycle is
423 quite constant at the different scales of aggregation (Figs. 8a,c). The majority of the RCMs also
424 reproduce a quite constant standard deviation, including those forced by IPSL-CMSA-MR, HadGEM2-
425 ES, and CNRM-CM5 that significantly underestimate it. In contrast, the regional simulations driven by
426 MPI-ESM-LR and EC-EARTH exhibit variable amplitudes at different scales and locations, suggesting
427 that performances of these models are affected by the scale of aggregation. However, this variability is
428 reduced as the grid spacing is reduced from EUR-44 to EUR-11. The centered RMSE is also quite
429 constant throughout scales and locations (Figs. 8b,d). Interestingly, when the spatial resolution is
430 increased, the RMSE of all models with positive CC tend to cluster around 15 mm.

431
432

433 **4.5 *Annual and Seasonal Trends in Observed and Simulated Time Series***

434 The presence and magnitude of annual trends at Full scale have been investigated by applying
435 the Mann-Kendall test and computing the slope of linear regression. Results are presented in Fig. 9 for
436 EUR-44, EUR-11, and corresponding observations. The slopes of linear trends are displayed on the left
437 (right) part of each panel if the trend was found to be not significant (significant) according to the
438 Mann-Kendall test at 95% confidence level. The observed records are characterized by a statistically
439 significant negative trend with slope of -3.4 mm/year. All GCM-RCM combinations underestimate the
440 observed trend, with most of the models displaying decreasing trends with absolute values lower than
441 2.3 mm/year. Moreover, although the majority of models simulate negative trends as the observations
442 (but smaller in magnitude), only two (NorESM1-M-RCA4 for EUR-44 and EC-EARTH-HIRHAM5
443 for EUR-11) of these are statistically significant at Full scale and also capture fairly well the observed
444 slope. On the contrary, some RCMs reproduce positive trends that, in one case, is statistically
445 significant (CNRM-CM5-RCA4 for EUR-11). The same discrepancy (positive trend) is also displayed
446 by some RCMs at certain scales and locations, which are statistically significant for the combination
447 CNRM-CM5-ALADIN52 at EUR-44 resolution at Quarter scale in SE (not shown) and for CNRM-
448 CM5-RCA4 at EUR-11 resolution at Full scale, Half scale in E, and Quarter scale in NW (not shown).

449 Fig. 10 displays the slope of the annual trends simulated by the GCM-RCM combinations
450 available at both EUR-44 and EUR-11 resolutions for the different scales of aggregation. Again, we
451 assume as reference the observed trends, which resulted always negative and statistically significant,
452 with larger absolute values in the eastern part of the island and, within this part, in the northern quarter.
453 Increasing the grid resolution does not have a significant impact on the models' ability to simulate the
454 slope, but it leads to an increasing number of negative trends that are statistically significant (listed in
455 caption of Fig. 10). Considering the effect of the aggregation scale, most models are able to capture the
456 relative changes of the trend magnitude (even if not statistically significant) from W to E at Half scale.

457 At Quarter scale, the models show instead all possible outcomes, including constant slope at all
458 locations, and slopes that are either positively or negatively correlated with the observed values.

459 The presence of trends in observed and GCM-RCM precipitation has been also investigated for
460 each season. Results for EUR-44, EUR-11 and observations at the Full scale are reported in Fig. 11.
461 Trends on observed P are negative for all seasons, except JJA (slope is ~ 0), while only for DJF we
462 found a statistically significant decline. Unfortunately, the majority of the models are not able to
463 capture the observed seasonal trend. At both grid resolutions, results of seasonal trends do not provide a
464 clear and coherent indication: in many cases, the same model simulates both positive and negative
465 trend slopes in different seasons, except in SON where they are mostly negative for both EUR-44 and
466 EUR-11 and statistically significant for about 40% of GCM-RCM combinations. Few cases of
467 statistically significant simulated trends are detected in MAM and JJA at both resolutions, and only one
468 in DJF for EUR-11. The analysis of seasonal trends provides also insight on the outcomes at annual
469 scale. For example, the combination NorESM1-M–RCA4 in EUR-44 reproduced very well statistical
470 significance and slope of the observed trend at annual scale. However, Fig. 11a shows that this model is
471 not able to capture the right season when the decline of P occurs, as it simulates a statistically
472 significant negative trend in spring instead of winter. As another example, the RCMs driven by
473 HadGEM2-ES are characterized, at both resolutions, by a negligible slope of the annual trend. As
474 shown in Fig. 11, this is explained by the combined effect of statistically significant increasing and
475 decreasing trends of ~ 4 mm/year simulated in MAM and SON, respectively. Finally, trends of seasonal
476 precipitation were also investigated across different scales of aggregation, leading to similar
477 considerations drawn at annual scale from the examination of Fig. 10. Results of this analysis are
478 shown for DJF in Fig. S4 of the supplementary materials, which reports the slopes of winter trends as a
479 function of the scales of aggregation (results for other seasons are similar and, thus, were not reported).

480
481

482 **4.6 Control of Driving GCM and Nested RCM on Simulated Precipitation**

483 As a next step, we assessed the relative importance of the driving GCM and nested RCM in the
484 simulation of the precipitation statistics investigated in the previous sections. With this aim, we applied
485 the ANOVA analysis described in Section 3.4. Fig. 12 shows the percent of variance explained by
486 RCM and GCM components, and their interaction (RCM-GCM), namely R, G and RG statistics
487 defined in equations (2-4), respectively, for: slope of linear regression between mean annual P and
488 elevation; spatial standard deviation of mean annual P at the original RCM resolutions; mean and CV
489 of annual P; CC between simulated and observed monthly P; mean DJF and JJA P; and slope of the
490 linear trend in annual P. Results are referred to the Full scale and are very similar at other scales. As
491 foreseen by the examination of Figs. 2 and 3, the ANOVA analysis clearly indicates that the orographic
492 control on annual P and its spatial variability are largely dominated by the RCM, whose importance
493 becomes higher as the grid spacing is reduced. The GCM explains instead most of the variance of the
494 mean annual P and its interannual variability (CV) at both resolutions, with larger importance of the
495 RCM for EUR-11 (~40%). As anticipated by the comments previously made on the clustering of
496 GCMs in Figs. 6 and 7, the metrics measuring the monthly variability and seasonal P are mostly
497 controlled by the GCM. The only exception is for summer P in EUR-11, where RCM and GCM have
498 similar importance. Somewhat unexpectedly, the largest percent of variance of the annual trend slope is
499 explained by the RCM for EUR 44 and it is equally associated to GCM and RCM for EUR-11. Finally,
500 we notice that, in all cases, the interaction term RG is always very small: as discussed in Déqué et al.
501 (2012), this drawback is mostly due to the assumption that $RG = 0$ in equation (5).

502 **5. Summary and Discussion**

503 In the following, we summarize the main outcomes of our work in the context of previous
504 studies focused on the Mediterranean region. While differences are expected when comparing analyses
505 based on various experimental settings and scales, the following discussion aims at providing
506
507

508 additional insight on the variability of climate models' performances across scales within large regions
509 with relatively similar climatic features. In addition, we provide guidance for the future use in Sardinia
510 of the GCM-RCM combinations of EURO-CORDEX analyzed here.

511

512 (1) The simulated spatial patterns of the climatological means are relatively well correlated with the
513 observation, except for a few cases, but the spatial variability is largely overestimated. Additionally, we
514 found that increasing the grid resolution from EUR-44 to EUR-11 leads to lower correlation
515 coefficients with the observed patterns. This suggests that the capacity of RCMs to capture smaller-
516 scale variations of climatological precipitation patterns is somewhat limited, even if their grid spacing
517 is reduced. Kotlarski et al. (2014) analyzed some of the GCM-RCM combinations of EURO-CORDEX
518 assessed here, but focusing on the entire Mediterranean area and using the "Evaluation" experiment
519 and the E-OBS reference dataset. Despite these differences, they also found a general overestimation of
520 the spatial variability. However, they did not detect appreciable differences between the patterns at the
521 two resolutions.

522

523 (2) The models tend to cluster around the observed mean annual P at different scales of aggregation
524 and locations, with positive and negative biases (reaching up to $\pm 60\%$). This is also true for the
525 interannual variability, expressed as CV of annual P, even if with a slight underestimation (bias from -
526 45% to +50%). In addition, we found that model biases decrease when considering simulations at
527 smaller grid spacing of EUR-11. Our findings differ from the analyses of Kotlarski et al. (2014), who
528 reported, for the Mediterranean region, positive biases up to +80% for mean annual P and did not find
529 improvements when simulations were conducted at higher spatial resolution. Similar model biases for
530 both EUR-44 and EUR-11 simulations were also found by Prein et al. (2016) when they were
531 computed over large regions in Europe. As a result, our finding indicates that results of analyses carried

532 out at local scale may be quite different from those performed over large domains where climatic
533 features are heterogeneous (like the Mediterranean region).

534

535 (3) The majority of the models reproduce the phase of the annual cycle, but they underestimate the
536 amplitude. The RCMs driven by CNRM-CM5 and HadGEM2-ES simulate instead a stationary
537 behavior of P throughout the year. For all models, errors are mostly due to the underestimation of
538 winter P and (in several cases, strong) overestimation of summer P. This is consistent with the analyses
539 of GCM outputs reported by Giorgi and Lionello (2008) in a sub-domain of the Mediterranean region
540 containing Sardinia. Deidda et al. (2013) found instead a general overestimation of P in all seasons by
541 the ENSEMBLES simulations in a watershed of $\sim 470 \text{ km}^2$ in southern Sardinia. A wet bias was also
542 found in both seasons by Kotlarski et al. (2014) over the whole Mediterranean area. In contrast, the
543 PRUDENCE simulations evaluated by Jacob et al. (2007) in the Mediterranean region underestimated
544 both summer and winter P. At seasonal scale, we could not identify clear improvements in model skill
545 between RCMs run at larger and smaller horizontal spacing. This finding differs from recent studies by
546 Torma et al. (2015) and Prein et al. (2016), who demonstrated that increasing the grid resolution of
547 CORDEX RCMs from 0.44° to 0.11° leads to improved skills in the reproduction of the seasonal P in
548 regions with complex terrain. Finally, we found that the GCM is the main factor controlling the
549 seasonal variability of P, as also reported by Deque et al. (2005) for PRUDENCE and ENSEMBLES
550 simulations. Overall, the large variety of similarities and discrepancies between our work and other
551 intercomparison studies suggests that the outcomes of the seasonal cycle analyses can be significantly
552 modified by the use of different GCM-RCM combinations, setup of climate experiments, extent of the
553 study region, and type of reference dataset.

554

555 (4) Observed P records in Sardinia show a statistically significant increase of annual P with elevation.

556 Fig. 2 and ANOVA results in Fig. 12 indicate that RCMs exert an orographic control of simulated
557 precipitation. At EUR-44 resolution, most models correctly capture the positive slope, but the
558 magnitude is highly overestimated. Three RCMs (CCLM4-8-17, ALADIN52, and REMO2009)
559 reproduce instead non-statistically significant decreasing relations. As a positive note, increasing the
560 grid resolution to EUR-11 dramatically improves the models' skill, including that of CCLM4-8-17.
561 This is corroborated by results of Kotlarski et al. (2014), who found that the CCLM model run at ~25-
562 km resolution (intermediate between EUR-44 and EUR-11) in the whole Mediterranean region is able
563 to reproduce a positive relation between P and elevation.

564

565 (5) Our observations also indicate the existence in Sardinia of a statistically significant decreasing trend
566 in annual P time series. A negative trend of P has been observed in other Mediterranean areas and
567 ascribed to an increase in the positive phase of the North Atlantic Oscillation during 1961–1990
568 (Hurrell, 1995). While a large portion of the models simulate declining P at annual scale, the rate of
569 precipitation decrease is always underestimated and, except for very few cases, trends are not
570 statistically significant at 95% confidence level (results are not markedly different even when
571 considering the 90% confidence level). Further investigations on modeled seasonal trends revealed that
572 annual precipitation decline can be mostly attributed to P diminishing in the fall season (instead of
573 winter, as suggested by the observations). Clustering of colors in Figs. 9 and 11 and results of the
574 ANOVA analysis indicate that GCMs control the trend. Somewhat unexpectedly, only very few studies
575 tested the skill of regional climate simulations to capture observed precipitation trends by analyzing
576 historical simulations, reporting contrasting outcomes. Giorgi et al. (2004) found the evidence of both
577 agreements and disagreements between observed and simulated P trends by two RCMs in Europe.
578 Giorgi and Lionello (2008) showed instead that an ensemble of GCMs fails in reproducing observed
579 seasonal declining P trends in the Mediterranean region, while Coppola and Giorgi (2010)

580 demonstrated qualitatively that a different ensemble of GCMs is able to capture seasonal declining
581 trends in northern Italy. An important reason that can explain these contrasting results and the
582 difficulties in evaluating the climate models' ability to capture observed trends is the role of the internal
583 climate variability. Its associated uncertainty, in fact, has been demonstrated to significantly affect the
584 analysis of trends in climate variables at global and regional scales (Deser et al., 2012, 2014). In this
585 work, we could not address this source of uncertainty because RCM simulations were only available
586 under one GCM realization, except for REMO2009 that was forced by two ensemble members of MPI-
587 ESM-LR (note that similar results were obtained in these two cases). As a consequence, our
588 conclusions cannot be considered definitive.

589

590 (6) The intercomparison analyses conducted here provide useful guidance for impact studies in the
591 island of Sardinia. To further support this aim, Fig. 13 shows the model ranks for four P properties
592 computed using the error metric of equation (6) that combined the variables listed in Table 5. The ranks
593 (whose values are listed in Tables S1-S4 of the supplementary materials) were calculated merging all
594 31 GCM-RCM combinations at EUR-44 and EUR-11 resolutions. The following considerations can be
595 made. (i) We consider the ability to simulate the orographic effect as the first screening criterion that
596 needs to be checked when selecting a model, as it evaluates an important aspect of the models' physics.
597 (ii) Increasing the grid resolution does not lead to consistently better or worse performances. (iii) The
598 effect of spatial aggregation is important for the interannual P variability, where the ranks of the same
599 model can significantly change across scales and locations (see, e.g., the simulations with REMO2009),
600 and less evident for seasonal variability and annual trend. (iv) No GCM-RCM combination exhibits
601 consistently higher or lower performances across the four examined P properties. As a consequence,
602 the selection of the best performing climate models depends on the scope and scale of the impact study.

603

604 **6. Conclusions**

605

606 We compared and evaluated performances of two ensembles of regional climate simulations at
607 0.44° and 0.11° grid resolution from the EURO-CORDEX initiative in reproducing the present-day
608 precipitation climatologies in the Mediterranean island of Sardinia. Two promising results include: (i)
609 the relatively high correlation between simulated and observed spatial patterns of the climatological
610 annual and seasonal means; and (ii) the marked improvement in the representation of orographic effects
611 on P found for the EUR-11 simulations. On the negative side, the models are characterized by different
612 types of deficiencies in the simulation of observed annual and seasonal trends, which is in our opinion
613 one of the most critical limitations that require further investigation. Our analyses also show that the set
614 of best performing models depends on the specific P property and scale of interest. The findings of this
615 work provide guidance to increase the utility of regional climate simulations for vulnerability, impact
616 and adaptation studies at local scales under future climate scenarios. Future work should be focused on
617 exploring the physical reasons leading to the model biases and on using this knowledge to inform bias
618 correction techniques (see, e.g., Addor et al., 2016).

619 **Acknowledgments**

620

621 We thank two anonymous reviewers, whose suggestions and comments helped to improve the
622 quality of the manuscript. This work has been funded by the Sardinia Region with Law 7/2007, funding
623 call 2013, project CRP 78576: “Anthropogenic and climatic impacts on the hydrological cycle at basin
624 and hillslope scale” (Impatti antropogenici e climatici sul ciclo idrologico a scala di bacino e di
625 versante). Outputs of climate models are available at: [http://www.euro-](http://www.euro-cordex.net/060378/index.php.en)
626 [cordex.net/060378/index.php.en](http://www.euro-cordex.net/060378/index.php.en). Precipitation observations are available at
627 <http://www.regione.sardegna.it/j/v/25?s=131338&v=2>.

References

- 630 Addor, N., Rohrer, M., Furrer, R., & Seibert, J. (2016). Propagation of biases in climate models from
631 the synoptic to the regional scale: Implications for bias adjustment. *Journal of Geophysical*
632 *Research: Atmospheres*, *121*(5), 2075-2089.
- 633 Alpert, P., Ben-Gai, T., Baharad, A., Benjamini, Y., Yekutieli, D., Colacino, M., . . . Manes, A. (2002).
634 The paradoxical increase of Mediterranean extreme daily rainfall in spite of decrease in total
635 values. *Geophysical Research Letters*, *29*(11), 31-31 - 31-34.
- 636 Amanatidis, G. T., Paliatsos, A. G., Repapis, C. C., & Bartzis, J. G. (1993). Decreasing precipitation
637 trend in the Marathon area, Greece. *International Journal of Climatology*, *13*(2), 191-201.
- 638 Arora, V. K., Scinocca, J. F., Boer, G. J., Christian, J. R., Denman, K. L., Flato, G. M., . . . Merryfield,
639 W. J. (2011). Carbon emission limits required to satisfy future representative concentration
640 pathways of greenhouse gases. *Geophysical Research Letters*, *38*(5).
641 doi:10.1029/2010gl046270
- 642 Baldauf, M., Seifert, A., Förstner, J., Majewski, D., Raschendorfer, M., & Reinhardt, T. (2011).
643 Operational convective-scale numerical weather prediction with the COSMO model:
644 Description and sensitivities. *Monthly Weather Review*, *139*(12), 3887-3905. doi:10.1175/mwr-
645 d-10-05013.1
- 646 Bentsen, M., Bethke, I., Debernard, J., Iversen, T., Kirkevåg, A., Seland, Ø., . . . Hoose, C. (2013). The
647 Norwegian earth system model, NorESM1-M—Part 1: description and basic evaluation of the
648 physical climate. *Geosci. Model Dev*, *6*(3), 687-720.
- 649 Bhatkoti, R., Moglen, G. E., Murray-Tuite, P. M., & Triantis, K. P. (2016). Changes to Bridge Flood
650 Risk under Climate Change. *Journal of Hydrologic Engineering*, *21*(12), 04016045.
- 651 Bird, D. N., Benabdallah, S., Gouda, N., Hummel, F., Koeberl, J., La Jeunesse, I., . . . Woess-Gallasch,
652 S. (2016). Modelling climate change impacts on and adaptation strategies for agriculture in
653 Sardinia and Tunisia using AquaCrop and value-at-risk. *Science of the Total Environment*, *543*,
654 1019-1027.
- 655 Bøssing Christensen, O., Drews, M., Hesselbjerg Christensen, J., Dethloff, K., Ketelsen, K., Hebestadt,
656 I., & Rinke, A. (2007). *The HIRHAM Regional Climate Model. Version 5 (beta)*. Retrieved
657 from
- 658 Cannarozzo, M., Noto, L. V., & Viola, F. (2006). Spatial distribution of rainfall trends in Sicily (1921-
659 2000). *Physics and Chemistry of the Earth*, *31*(18), 1201-1211. doi:10.1016/j.pce.2006.03.022
- 660 Chessa, P., Cesari, D., & Delitala, A. (1999). Mesoscale precipitation and temperature regimes in
661 Sardinia (Italy) and their related synoptic circulation. *Theoretical and Applied Climatology*,
662 *63*(3), 195-221.
- 663 Chessa, P., Ficca, G., Marrocu, M., & Buizza, R. (2004). Application of a limited-area short-range
664 ensemble forecast system to a case of heavy rainfall in the Mediterranean region. *Weather and*
665 *forecasting*, *19*(3), 566-581.
- 666 Christensen, J. H., Carter, T. R., Rummukainen, M., & Amanatidis, G. (2007). Evaluating the
667 performance and utility of regional climate models: the PRUDENCE project. *Climatic Change*,
668 *81*, 1-6.
- 669 Colin, J., Déqué, M., Radu, R., & Somot, S. (2010). Sensitivity study of heavy precipitation in Limited
670 Area Model climate simulations: influence of the size of the domain and the use of the spectral
671 nudging technique. *Tellus A*, *62*(5), 591-604.
- 672 Collins, W., Bellouin, N., Doutriaux-Boucher, M., Gedney, N., Halloran, P., Hinton, T., . . . Liddicoat,
673 S. (2011). Development and evaluation of an Earth-System model-HadGEM2. *Geoscientific*

674 *Model Development*, 4(4), 1051.

675 Cook, B. I., Anchukaitis, K. J., Touchan, R., Meko, D. M., & Cook, E. R. (2016). Spatiotemporal
676 drought variability in the Mediterranean over the last 900 years. *Journal of Geophysical*
677 *Research: Atmospheres*.

678 Coppola, E., & Giorgi, F. (2010). An assessment of temperature and precipitation change projections
679 over Italy from recent global and regional climate model simulations. *International Journal of*
680 *Climatology*, 30(1), 11-32.

681 De Luís, M., Raventós, J., González-Hidalgo, J. C., Sánchez, J. R., & Cortina, J. (2000). Spatial
682 analysis of rainfall trends in the region of Valencia (East Spain). *International Journal of*
683 *Climatology*, 20(12), 1451-1469. doi:10.1002/1097-0088(200010)20:12<1451::aid-
684 joc547>3.0.co;2-0

685 Dee, D., Uppala, S., Simmons, A., Berrisford, P., Poli, P., Kobayashi, S., . . . Bauer, P. (2011). The
686 ERA-Interim reanalysis: Configuration and performance of the data assimilation system.
687 *Quarterly Journal of the Royal Meteorological Society*, 137(656), 553-597.

688 Deidda, R., Marrocu, M., Caroletti, G., Pusceddu, G., Langousis, A., Lucarini, V., . . . Speranza, A.
689 (2013). Regional climate models' performance in representing precipitation and temperature
690 over selected Mediterranean areas. *Hydrology and Earth System Sciences*, 17(12), 5041.

691 Deque, M., Jones, R., Wild, M., Giorgi, F., Christensen, J., Hassell, D., . . . Kjellström, E. (2005).
692 Global high resolution vs. regional climate model climate change scenarios over Europe:
693 Quantifying confidence level from PRUDENCE results. *Clim. Dyn.*, 25, 653-670.

694 Déqué, M., Somot, S., Sanchez-Gomez, E., Goodess, C., Jacob, D., Lenderink, G., & Christensen, O.
695 (2012). The spread amongst ENSEMBLES regional scenarios: regional climate models, driving
696 general circulation models and interannual variability. *Climate dynamics*, 38(5-6), 951-964.

697 Deser, C., Phillips, A., Bourdette, V., & Teng, H. (2012). Uncertainty in climate change projections:
698 the role of internal variability. *Climate dynamics*, 38(3-4), 527-546.

699 Deser, C., Phillips, A. S., Alexander, M. A., & Smoliak, B. V. (2014). Projecting North American
700 climate over the next 50 years: Uncertainty due to internal variability. *Journal of Climate*,
701 27(6), 2271-2296.

702 Dunne, J. P., John, J. G., Adcroft, A. J., Griffies, S. M., Hallberg, R. W., Shevliakova, E., . . . Harrison,
703 M. J. (2012). GFDL's ESM2 global coupled climate-carbon earth system models. Part I:
704 Physical formulation and baseline simulation characteristics. *Journal of Climate*, 25(19), 6646-
705 6665.

706 Ehmele, F., Barthlott, C., & Corsmeier, U. (2015). The influence of Sardinia on Corsican rainfall in the
707 western Mediterranean Sea: A numerical sensitivity study. *Atmospheric Research*, 153, 451-
708 464.

709 Esteban-Parra, M. J., Rodrigo, F. S., & Castro-Diez, Y. (1998). Spatial and temporal patterns of
710 precipitation in Spain for the period 1880-1992. *International Journal of Climatology*, 18(14),
711 1557-1574.

712 Gascón, E., Laviola, S., Merino, A., & Miglietta, M. (2016). Analysis of a localized flash-flood event
713 over the central Mediterranean. *Atmospheric Research*, 182, 256-268.

714 Giorgetta, M. A., Jungclaus, J., Reick, C. H., Legutke, S., Bader, J., Böttinger, M., . . . Fieg, K. (2013).
715 Climate and carbon cycle changes from 1850 to 2100 in MPI-ESM simulations for the Coupled
716 Model Intercomparison Project phase 5. *Journal of Advances in Modeling Earth Systems*, 5(3),
717 572-597.

718 Giorgi, F. (2006). Climate change hot-spots. *Geophysical Research Letters*, 33(8), 4.
719 doi:10.1029/2006GL025734

720 Giorgi, F., Bi, X., & Pal, J. (2004). Mean, interannual variability and trends in a regional climate
721 change experiment over Europe. II: climate change scenarios (2071–2100). *Climate dynamics*,

722 23(7-8), 839-858.

723 Giorgi, F., & Gutowski Jr, W. J. (2015). Regional dynamical downscaling and the CORDEX initiative.

724 *Annual Review of Environment and Resources*, 40, 467-490.

725 Giorgi, F., & Lionello, P. (2008). Climate change projections for the Mediterranean region. *Global and*

726 *Planetary Change*, 63(2), 90-104.

727 Giorgi, F., & Mearns, L. O. (1999). Introduction to special section: Regional climate modeling

728 revisited. *Journal of Geophysical Research: Atmospheres*, 104(D6), 6335-6352.

729 Godart, A., Anquetin, S., Leblois, E., & Creutin, J.-D. (2011). The contribution of orographically

730 driven banded precipitation to the rainfall climatology of a Mediterranean region. *Journal of*

731 *Applied Meteorology and Climatology*, 50(11), 2235-2246.

732 Gonzalez-Hidalgo, J. C., Lopez-Bustins, J. A., Štěpánek, P., Martin-Vide, J., & de Luis, M. (2009).

733 Monthly precipitation trends on the Mediterranean fringe of the Iberian Peninsula during the

734 second-half of the twentieth century (1951-2000). *International Journal of Climatology*, 29(10),

735 1415-1429. doi:10.1002/joc.1780

736 Hanel, M., & Buishand, T. A. (2011). Analysis of precipitation extremes in an ensemble of transient

737 regional climate model simulations for the Rhine basin. *Climate dynamics*, 36(5-6), 1135-1153.

738 Haylock, M., Hofstra, N., Klein Tank, A., Klok, E., Jones, P., & New, M. (2008). A European daily

739 high-resolution gridded data set of surface temperature and precipitation for 1950–2006.

740 *Journal of Geophysical Research: Atmospheres*, 113(D20).

741 Hazeleger, W., Wang, X., Severijns, C., Ștefănescu, S., Bintanja, R., Sterl, A., . . . Van den Hurk, B.

742 (2012). EC-Earth V2. 2: description and validation of a new seamless earth system prediction

743 model. *Climate dynamics*, 39(11), 2611-2629.

744 Heinrich, G., Gobiet, A., & Mendlik, T. (2014). Extended regional climate model projections for

745 Europe until the mid-twentyfirst century: combining ENSEMBLES and CMIP3. *Climate*

746 *dynamics*, 42(1-2), 521-535.

747 Hourdin, F., Foujols, M.-A., Codron, F., Guemas, V., Dufresne, J.-L., Bony, S., . . . Ghattas, J. (2013).

748 Impact of the LMDZ atmospheric grid configuration on the climate and sensitivity of the IPSL-

749 CM5A coupled model. *Climate dynamics*, 40(9-10), 2167-2192.

750 Hurrell, J. (1995). Decadal trends in the North Atlantic Oscillation: regional temperatures and

751 precipitation *Science* 269, 676-679.

752 Jacob, D., Bärring, L., Christensen, O. B., Christensen, J. H., de Castro, M., Deque, M., . . . Jones, R.

753 (2007). An inter-comparison of regional climate models for Europe: model performance in

754 present-day climate. *Climatic Change*, 81, 31-52.

755 Jacob, D., Petersen, J., Eggert, B., Alias, A., Christensen, O. B., Bouwer, L. M., . . . Georgievski, G.

756 (2014). EURO-CORDEX: new high-resolution climate change projections for European impact

757 research. *Regional Environmental Change*, 14(2), 563-578.

758 Jeffrey, S., Rotstayn, L., Collier, M., Dravitzki, S., Hamalainen, C., Moeseneder, C., . . . Syktus, J.

759 (2013). Australia's CMIP5 submission using the CSIRO Mk3. 6 model. *Aust. Meteor.*

760 *Oceanogr. J.*, 63, 1-13.

761 Kendall, M. G. (1962). *Rank correlation methods*. New York: Hafner Publishing Company.

762 Kjellström, E., Thejll, P., Rummukainen, M., Christensen, J. H., Boberg, F., Christensen, O. B., &

763 Maule, C. F. (2013). Emerging regional climate change signals for Europe under varying large-

764 scale circulation conditions. *Clim. Res.*, 56(2), 103-119.

765 Kotlarski, S., Keuler, K., Christensen, O. B., Colette, A., Déqué, M., Gobiet, A., . . . van Meijgaard, E.

766 (2014). Regional climate modeling on European scales: a joint standard evaluation of the

767 EURO-CORDEX RCM ensemble. *Geoscientific Model Development*, 7(4), 1297-1333.

768 Kuo, C.-C., & Gan, T. Y. (2015). Risk of Exceeding Extreme Design Storm Events under Possible

769 Impact of Climate Change. *Journal of Hydrologic Engineering*, 20(12), 04015038.

770 Kutiel, H., Maheras, P., & Guika, S. (1996). Circulation and extreme rainfall conditions in the eastern
771 mediterranean during the last century. *International Journal of Climatology*, 16(1), 73-92.

772 Lázaro, R., Rodrigo, F. S., Gutiérrez, L., Domingo, F., & Puigdefábregas, J. (2001). Analysis of a 30-
773 year rainfall record (1967-1997) in semi-arid SE Spain for implications on vegetation. *Journal*
774 *of Arid Environments*, 48(3), 373-395. doi:10.1006/jare.2000.0755

775 Lionello, P., Malanotte-Rizzoli, P., Boscolo, R., Alpert, P., Artale, V., Li, L., . . . Tsimplis, M. (2006).
776 The Mediterranean climate: an overview of the main characteristics and issues. In: Elsevier.

777 Lorenz, P., & Jacob, D. (2010). Validation of temperature trends in the ENSEMBLES regional climate
778 model runs driven by ERA40. *Climate Research*, 44(2/3), 167-177.

779 Lucarini, V., Danihlik, R., Kriegerova, I., & Speranza, A. (2007). Does the Danube exist? Versions of
780 reality given by various regional climate models and climatological data sets. *Journal of*
781 *Geophysical Research: Atmospheres*, 112(D13).

782 Ludwig, R., & Roson, R. (2016). Climate change, water and security in the Mediterranean:
783 Introduction to the special issue. In.

784 Mann, H. B. (1945). Non parametric tests against trend. *Econometrica*, 13, 245-259.

785 Mascaro, G., Deidda, R., & Hellies, M. (2013). On the nature of rainfall intermittency as revealed by
786 different metrics and sampling approaches. *Hydrology and Earth System Sciences*, 17(1), 355.

787 Mascaro, G., White, D., Westerhoff, P., & Bliss, N. (2015). Performance of the CORDEX-Africa
788 regional climate simulations in representing the hydrological cycle of the Niger River basin.
789 *Journal of Geophysical Research: Atmospheres*, 120(24), 12425-12444.

790 Nikulin, G., Jones, C., Giorgi, F., Asrar, G., Büchner, M., Cerezo-Mota, R., . . . Hänsler, A. (2012).
791 Precipitation climatology in an ensemble of CORDEX-Africa regional climate simulations.
792 *Journal of Climate*, 25(18), 6057-6078.

793 Norrant, C., & Douguédroit, A. (2006). Monthly and daily precipitation trends in the Mediterranean
794 (1950-2000). *Theoretical and Applied Climatology*, 83(1-4), 89-106. doi:10.1007/s00704-005-
795 0163-y

796 Ozturk, T., Ceber, Z. P., Türkeş, M., & Kurnaz, M. L. (2015). Projections of climate change in the
797 Mediterranean Basin by using downscaled global climate model outputs. *International Journal*
798 *of Climatology*, 35(14), 4276-4292.

799 Piervitali, E., Colacino, M., & Conte, M. (1998). Rainfall over the central-western mediterranean basin
800 in the period 1951-1995. Part I: Precipitation trends. *Nuovo Cimento della Societa Italiana di*
801 *Fisica C*, 21(3), 331-344.

802 Piras, M., Mascaro, G., Deidda, R., & Vivoni, E. (2014). Quantification of hydrologic impacts of
803 climate change in a Mediterranean basin in Sardinia, Italy, through high-resolution simulations.
804 *Hydrology and Earth System Sciences*, 18(12), 5201-5217.

805 Piras, M., Mascaro, G., Deidda, R., & Vivoni, E. R. (2016). Impacts of climate change on precipitation
806 and discharge extremes through the use of statistical downscaling approaches in a
807 Mediterranean basin. *Science of the Total Environment*, 543, 952-964.

808 Prein, A., & Gobiet, A. (2017). Impacts of uncertainties in European gridded precipitation observations
809 on regional climate analysis. *International Journal of Climatology*, 37(1), 305-327.

810 Prein, A., Gobiet, A., Truhetz, H., Keuler, K., Goergen, K., Teichmann, C., . . . Nikulin, G. (2016).
811 Precipitation in the EURO-CORDEX 0.11° and 0.44° simulations: high resolution, high
812 benefits? *Climate dynamics*, 46(1-2), 383-412.

813 Rockel, B., Will, A., & Hense, A. (2008). The regional climate model COSMO-CLM (CCLM).
814 *Meteorologische Zeitschrift*, 17(4), 347-348.

815 Samuelsson, P., Jones, C. G., Willén, U., Ullerstig, A., Gollvik, S., Hansson, U., . . . Wyser, K. (2011).
816 The Rossby Centre Regional Climate model RCA3: model description and performance. *Tellus*
817 *A*, 63(1), 4-23.

- 818 Senatore, A., Mendicino, G., Smiatek, G., & Kunstmann, H. (2011). Regional climate change
819 projections and hydrological impact analysis for a Mediterranean basin in Southern Italy.
820 *Journal of Hydrology*, 399(1), 70-92.
- 821 Silvestro, F., Gabellani, S., Giannoni, F., Parodi, A., Rebori, N., Rudari, R., & Siccardi, F. (2012). A
822 hydrological analysis of the 4 November 2011 event in Genoa. *Natural Hazards and Earth
823 System Sciences*, 12(9), 2743.
- 824 Soddu, A., Deidda, R., Marrocu, M., Meloni, R., Paniconi, C., Ludwig, R., . . . Perra, E. (2013).
825 Climate variability and durum wheat adaptation using the AquaCrop model in southern
826 Sardinia. *Procedia Environmental Sciences*, 19, 830-835.
- 827 Sulis, M., Paniconi, C., Marrocu, M., Huard, D., & Chaumont, D. (2012). Hydrologic response to
828 multimodel climate output using a physically based model of groundwater/surface water
829 interactions. *Water Resources Research*, 48(12).
- 830 Sulis, M., Paniconi, C., Rivard, C., Harvey, R., & Chaumont, D. (2011). Assessment of climate change
831 impacts at the catchment scale with a detailed hydrological model of surface-subsurface
832 interactions and comparison with a land surface model. *Water Resources Research*, 47(1).
- 833 Tarolli, P., Borga, M., Morin, E., & Delrieu, G. (2012). Analysis of flash flood regimes in the North-
834 Western and South-Eastern Mediterranean regions. *Natural Hazards and Earth System
835 Sciences*, 12(5), 1255-1265.
- 836 Taylor, K. E. (2001). Summarizing multiple aspects of model performance in a single diagram. *Journal
837 of Geophysical Research: Atmospheres*, 106(D7), 7183-7192.
- 838 Taylor, K. E., Stouffer, R. J., & Meehl, G. A. (2012). An overview of CMIP5 and the experiment
839 design. *Bulletin of the American Meteorological Society*, 93(4), 485-498.
- 840 Teichmann, C., Eggert, B., Elizalde, A., Haensler, A., Jacob, D., Kumar, P., . . . Remedio, A. R. (2013).
841 How does a regional climate model modify the projected climate change signal of the driving
842 GCM: a study over different CORDEX regions using REMO. *Atmosphere*, 4(2), 214-236.
- 843 Torma, C., Giorgi, F., & Coppola, E. (2015). Added value of regional climate modeling over areas
844 characterized by complex terrain—Precipitation over the Alps. *Journal of Geophysical
845 Research: Atmospheres*, 120(9), 3957-3972.
- 846 Trambly, Y., Ruelland, D., Somot, S., Bouaicha, R., & Servat, E. (2013). High-resolution Med-
847 CORDEX regional climate model simulations for hydrological impact studies: a first evaluation
848 of the ALADIN-Climate model in Morocco. *Hydrology and Earth System Sciences*, 17(10),
849 3721.
- 850 Trigo, I. F., Davies, T. D., & Bigg, G. R. (2000). Decline in Mediterranean rainfall caused by
851 weakening of Mediterranean cyclones. *Geophysical Research Letters*, 27(18), 2913-2916.
852 doi:10.1029/2000gl011526
- 853 Türkeş, M. (1996). Spatial and temporal analysis of annual rainfall variations in Turkey. *International
854 Journal of Climatology*, 16(9), 1057-1076.
- 855 van der Linden, P., & Mitchell, J., editors. (2009). ENSEMBLES: Climate change and its impacts-
856 Summary of research and results from the ENSEMBLES project.
- 857 Van Meijgaard, E., Van Ulft, L., Van de Berg, W., Bosveld, F., Van den Hurk, B., Lenderink, G., &
858 Siebesma, A. (2008). The KNMI regional atmospheric climate model RACMO version 2.1.
859 *Koninklijk Nederlands Meteorologisch Instituut*.
- 860 Van Vuuren, D. P., Edmonds, J., Kainuma, M., Riahi, K., Thomson, A., Hibbard, K., . . . Lamarque, J.-
861 F. (2011). The representative concentration pathways: an overview. *Climatic Change*, 109(1-2),
862 5.
- 863 Viola, F., Caracciolo, D., Pumo, D., Noto, L., & La Loggia, G. (2014). Future Climate Forcings and
864 Olive Yield in a Mediterranean Orchard. *Water*, 6(6), 1562-1580.
- 865 Viola, F., Francipane, A., Caracciolo, D., Pumo, D., La Loggia, G., & Noto, L. V. (2016). Co-evolution

866 of hydrological components under climate change scenarios in the Mediterranean area. *Science*
867 *of the Total Environment*, 544, 515-524.

868 Voltaire, A., Sanchez-Gomez, E., y Méliá, D. S., Decharme, B., Cassou, C., Sénési, S., . . . Chevallier,
869 M. (2013). The CNRM-CM5. 1 global climate model: description and basic evaluation. *Climate*
870 *dynamics*, 40(9-10), 2091-2121.

871 Voloudakis, D., Karamanos, A., Economou, G., Kalivas, D., Vahamidis, P., Kotoulas, V., . . . Zerefos,
872 C. (2015). Prediction of climate change impacts on cotton yields in Greece under eight climatic
873 models using the AquaCrop crop simulation model and discriminant function analysis.
874 *Agricultural Water Management*, 147, 116-128.

875 Watanabe, M., Suzuki, T., O'ishi, R., Komuro, Y., Watanabe, S., Emori, S., . . . Sekiguchi, M. (2010).
876 Improved climate simulation by MIROC5: mean states, variability, and climate sensitivity.
877 *Journal of Climate*, 23(23), 6312-6335.

878
879

880 **Figure Captions**

881

882 **Figure 1.** (a) EURO-CORDEX domain with indication of the study area. (b) Digital elevation model of
883 Sardinia (Italy) with location of the rain gauges. (c) Grid points of EUR-44 in the rotated coordinate
884 system adopted by CORDEX and grid points of the regular grid at 0.5° (~50 km) resolution used to
885 interpolate the data. (d) Same as (c) but for EUR-11 where the interpolated grid has a resolution of 0.1°
886 (~10 km).

887

888 **Figure 2.** (a),(c) Relation between mean annual P observed and simulated by the GCM-RCM
889 combinations of (a) EUR-44 and (c) EUR-11 and the corresponding elevation. (b),(d) Slope of the
890 linear regressions for (b) EUR-44 and (d) EUR-11. In (b) and (d), the vertical dashed lines indicate the
891 presence of a linear relation that is statistically significant at 95%.

892

893 **Figure 3.** Normalized Taylor diagrams comparing the spatial patterns of (a-b) mean annual P, (c-d)
894 mean DJF P, and (e-f) mean JJA P. Results are shown for EUR-44 [EUR-11] in (a), (c) and (e) [(b),
895 (d), and (f)]. In each panel, the black star refers to the observed value where the normalized spatial
896 standard deviation is equal to 1, the radial distance from the black star quantifies the centered RSME
897 normalized by the observed spatial standard deviation, the azimuth and the radial distance from the
898 origin quantify instead CC and normalized spatial standard deviation, respectively. The observed
899 spatial deviations are 82, 30, and 11 mm (126, 51, 12 mm) at annual, winter and summer scales for
900 EUR-44 (EUR-11).

901

902 **Figure 4.** Relation between the mean annual P and CV for GCM-RCM combinations of (a) EUR-44
903 and (b) EUR-11 and observation aggregated at Full scale.

904

905 **Figure 5.** Relative bias in the simulation of mean annual P and CV at different aggregation scales and
906 locations for the GCM-RCM combinations available for both EUR-44 and EUR-11. In (a) and (b) [(c)
907 and (d)], results are shown for EUR-44 [EUR-11] for mean annual P and CV, respectively.

908

909 **Figure 6.** Climatological monthly means of P for observations and GCM-RCM combinations of (a)
910 EUR-44 and (b) EUR-11 aggregated at Full scale.

911

912 **Figure 7** Temporal Taylor diagram and seasonal bias computed for the GCM-RCM combinations of
913 (a,b) EUR-44 and (c,d) EUR-11 aggregated at Full scale.

914

915 **Figure 8.** Standard deviation and centered RMSE between simulated and observed monthly P at
916 different aggregation scales and locations for the GCM-RCM combinations available for both EUR-44
917 and EUR-11. In (a) and (b) [(c) and (d)], results are shown for EUR-44 [EUR-11] for CC and RMSE,
918 respectively.

919

920 **Figure 9.** Slope of the linear trend for annual P observed and simulated at Full scale by the GCM-RCM
921 combinations of (a) EUR-44 and (b) EUR-11. In each panel, the cases with significant (S) and non-
922 significant (N) trends at 5% significance level are plotted to the left and right of the dashed line,
923 respectively.

924

925 **Figure 10.** Slope of the linear trend for annual P observed and simulated at different aggregation scales
926 and locations for the GCM-RCM combinations available for both (a) EUR-44 and (b) EUR-11. The
927 observed trend is statistically significant in all cases. The simulated trends are never statistically
928 significant except the following cases. For EUR-44: EC-EARTH–HIRHAM at Quarter scale in NE.
929 For EUR-11: EC-EARTH–HIRHAM at Full scale, Half scale in W and Quarter scale in SE;
930 HadGEM2-ES–RACMO22E at Half scale in W and Quarter scale in SE; and CNRM-CM5–RCA4 at
931 Full scale, Half scale in E, and Quarter scale in NW.

932

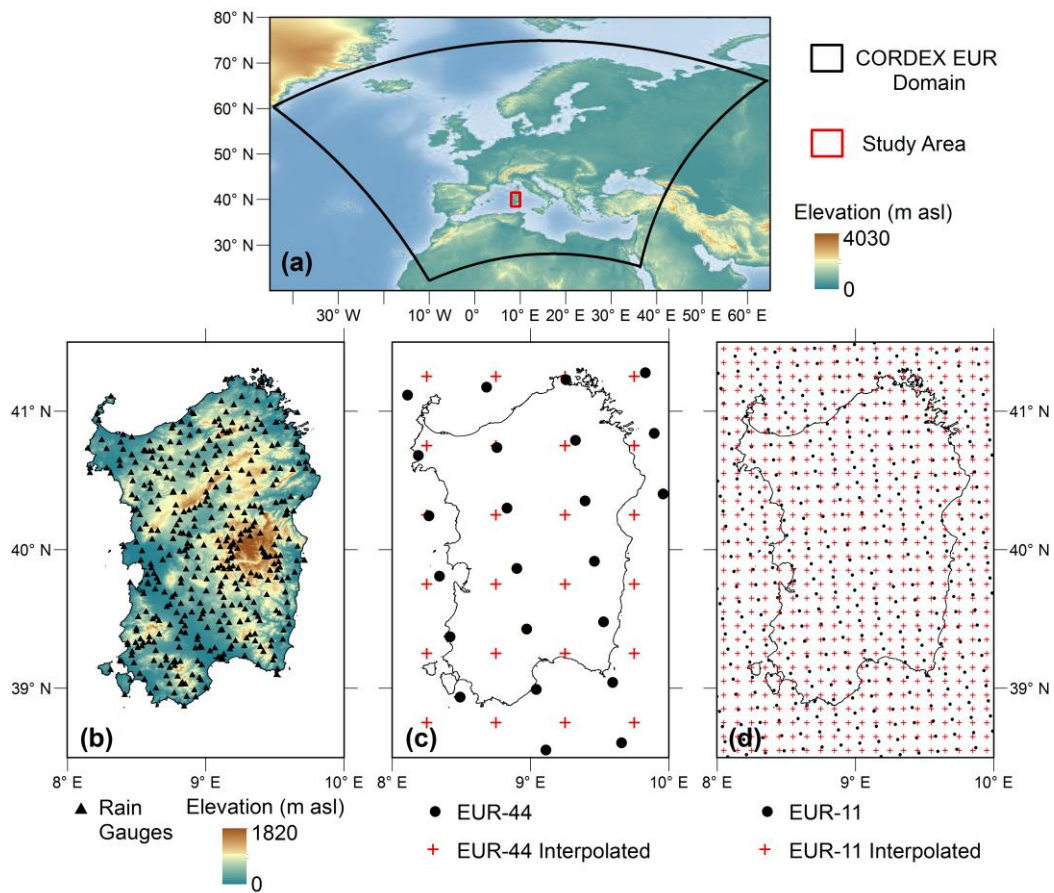
933 **Figure 11.** Slope of the linear trend for the mean seasonal P observed and simulated at Full scale by the
934 GCM-RCM combinations of (a) EUR-44 and (b) EUR-11. In each panel, the cases with significant (S)
935 and non-significant (N) trends at 5% significance level are plotted to the left and right of each season,
936 respectively.

937

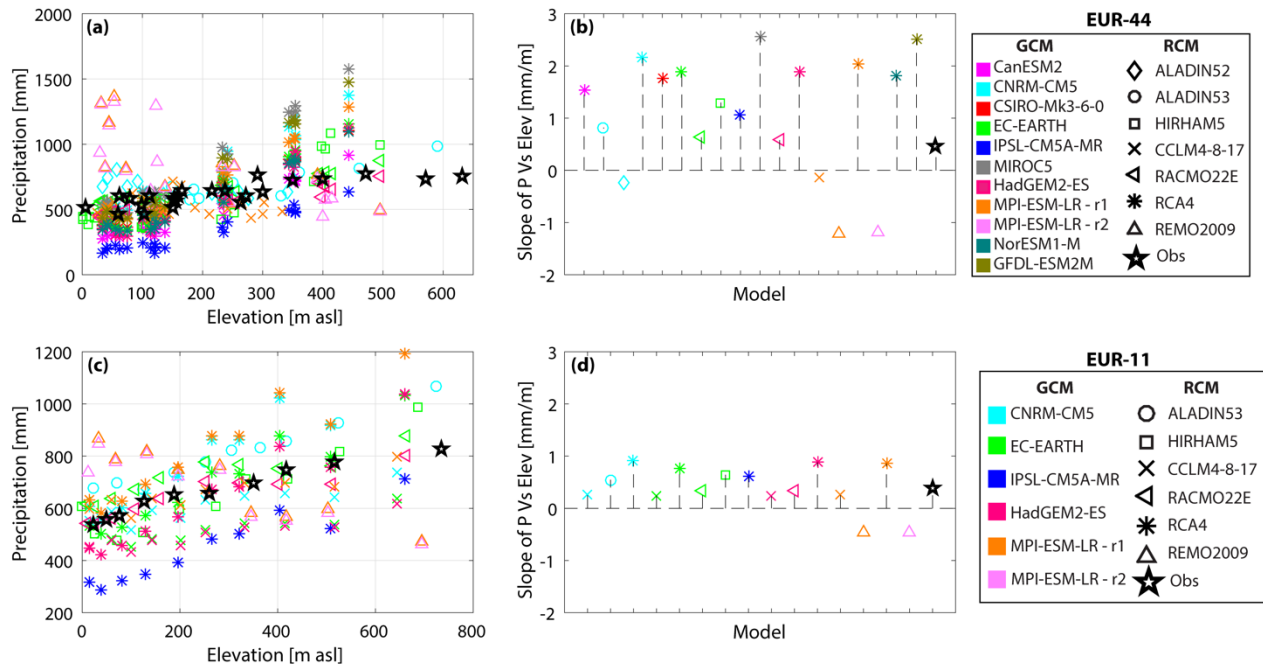
938 **Figure 12.** Percent of variance explained by RCM, GCM, and interaction between them (GCM-RCM)
939 for a number of simulated variable (see main text for details).

940

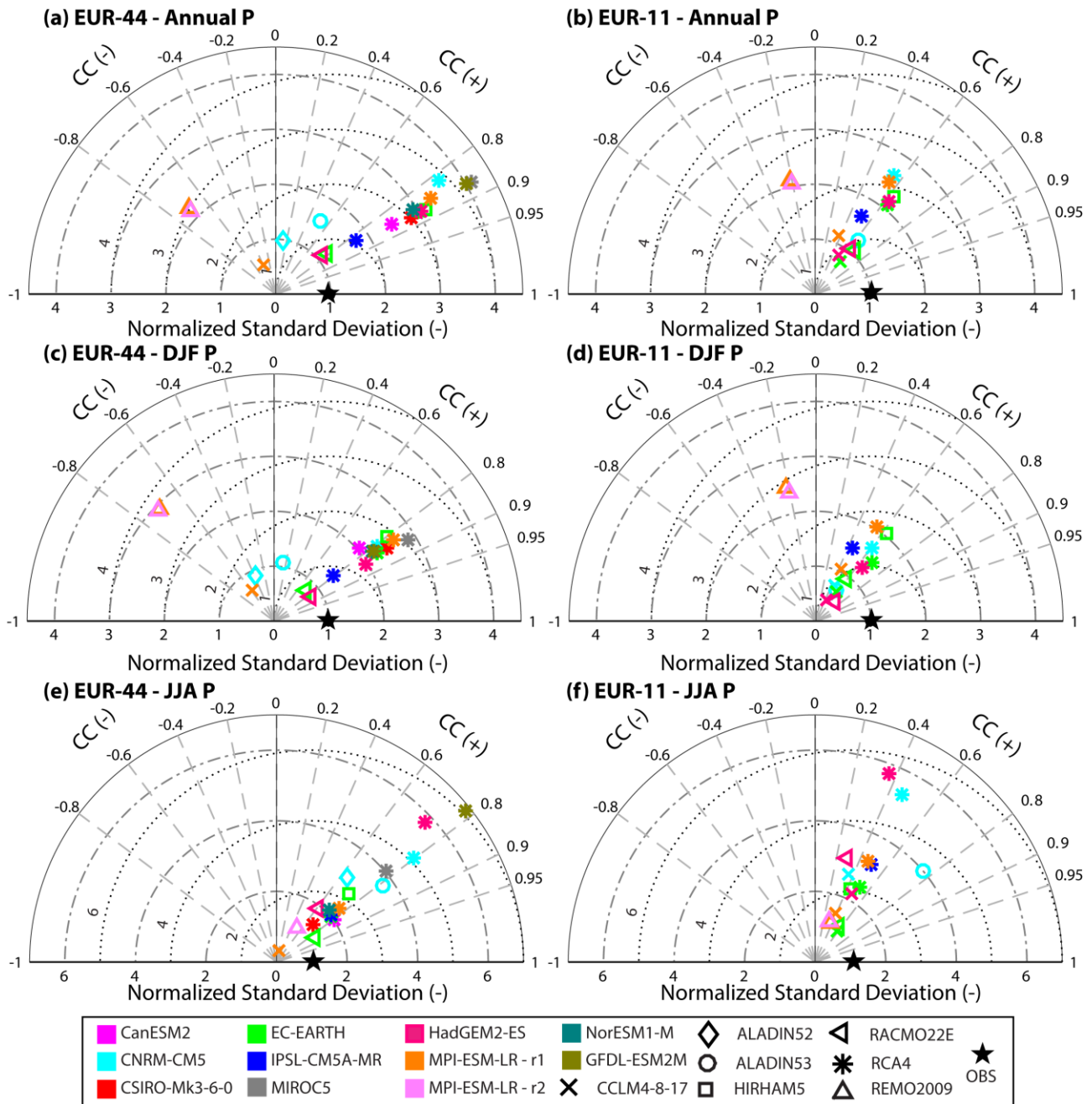
941 **Figure 13.** Ranks of the relative error ε_j defined in equation (6) and Table 5 for four P properties.
942 “Orog” is the orographic effect on P (see Table 5 for the variables considered in error computation of
943 each property).



944
 945 **Figure 1.** (a) EURO-CORDEX domain with indication of the study area. (b) Digital elevation model of
 946 Sardinia (Italy) with location of the rain gauges. (c) Grid points of EUR-44 in the rotated coordinate
 947 system adopted by CORDEX and grid points of the regular grid at 0.5° (~50 km) resolution used to
 948 interpolate the data. (d) Same as (c) but for EUR-11 where the interpolated grid has a resolution of 0.1°
 949 (~10 km).
 950

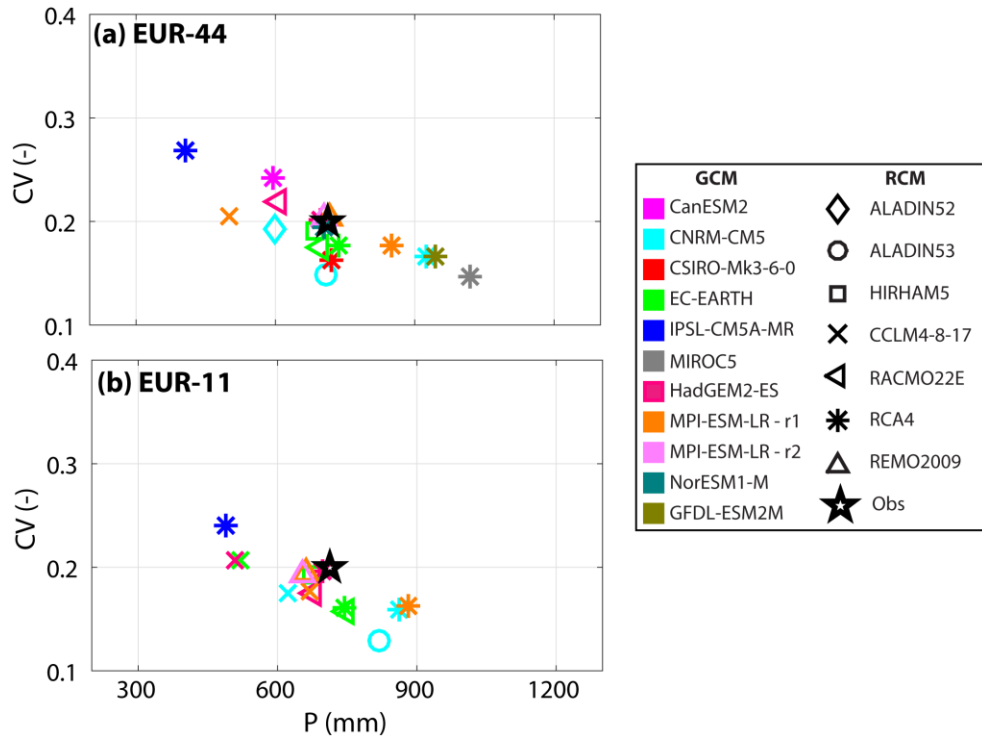


951
 952 **Figure 2.** (a),(c) Relation between mean annual P observed and simulated by the GCM-RCM
 953 combinations of (a) EUR-44 and (c) EUR-11 and the corresponding elevation. (b),(d) Slope of the
 954 linear regressions for (b) EUR-44 and (d) EUR-11. In (b) and (d), the vertical dashed lines indicate the
 955 presence of a linear relation that is statistically significant at 95%.
 956

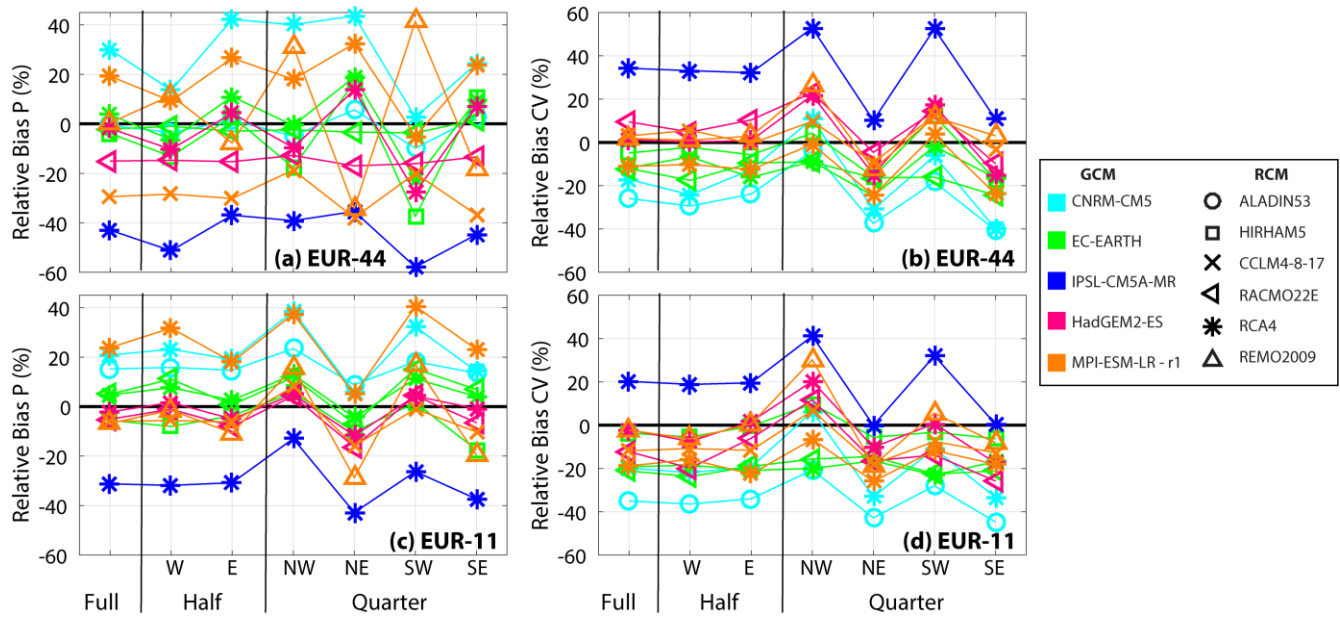


957

958 **Figure 3.** Normalized Taylor diagrams comparing the spatial patterns of (a-b) mean annual P, (c-d)
 959 mean DJF P, and (e-f) mean JJA P. Results are shown for EUR-44 [EUR-11] in (a), (c) and (e) [(b),
 960 (d), and (f)]. In each panel, the black star refers to the observed value where the normalized spatial
 961 standard deviation is equal to 1, the radial distance from the black star quantifies the centered RSME
 962 normalized by the observed spatial standard deviation, the azimuth and the radial distance from the
 963 origin quantify instead CC and normalized spatial standard deviation, respectively. The observed
 964 spatial deviations are 82, 30, and 11 (126, 51, and 12 mm) at annual, winter and summer scales for
 965 EUR-44 (EUR-11).

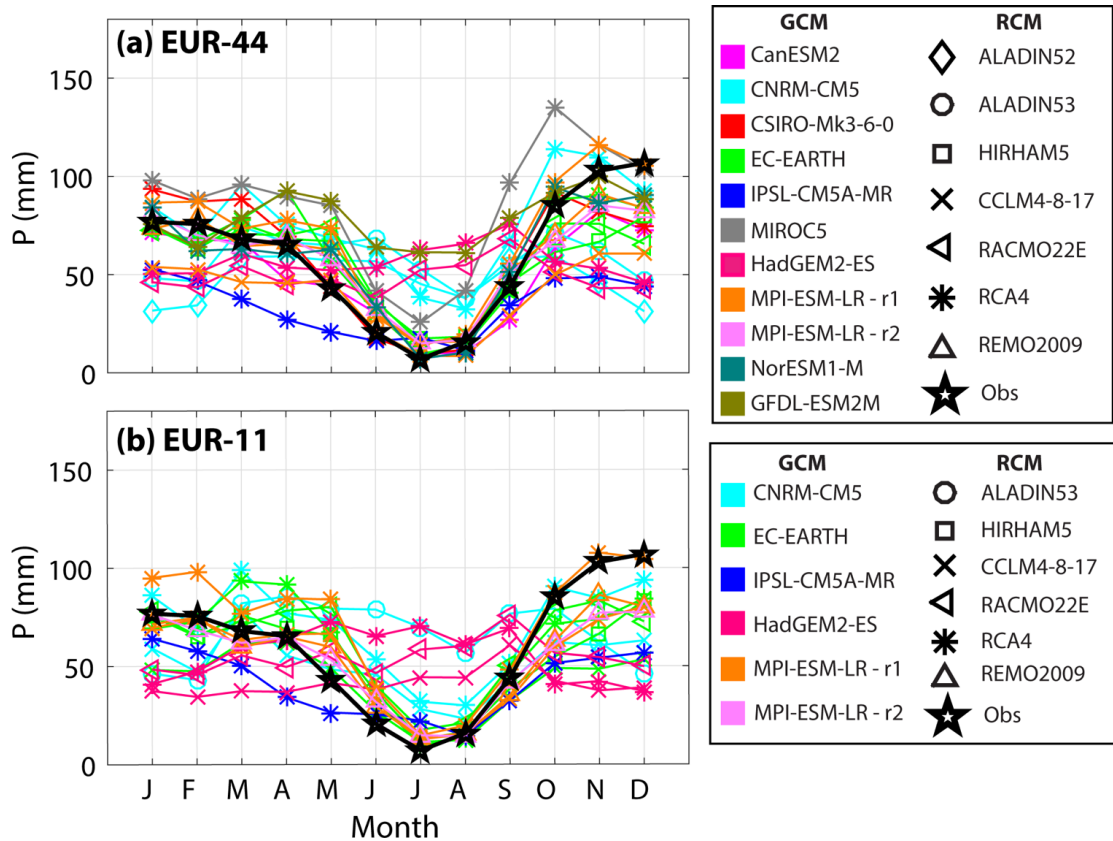


966
 967 **Figure 4.** Relation between the mean annual P and CV for GCM-RCM combinations of (a) EUR-44
 968 and (b) EUR-11 and observation aggregated at Full scale.



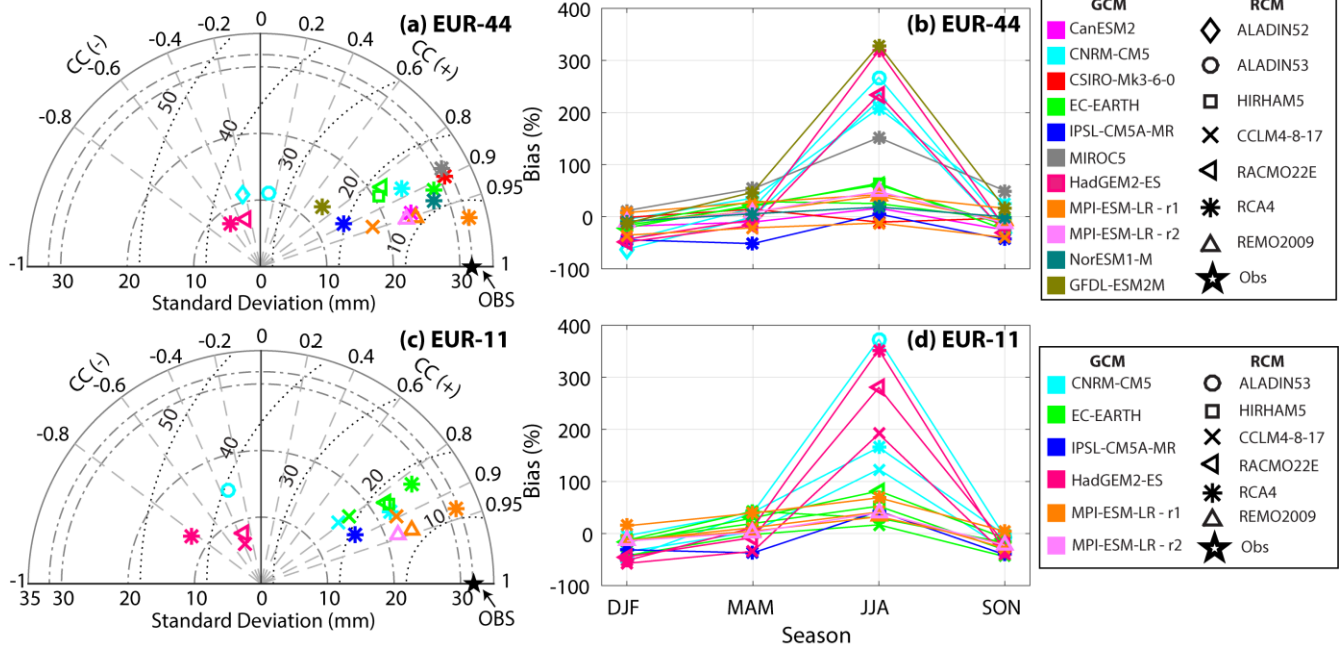
969
 970
 971
 972
 973

Figure 5. Relative bias in the simulation of mean annual P and CV at different aggregation scales and locations for the GCM-RCM combinations available for both EUR-44 and EUR-11. In (a) and (b) [(c) and (d)], results are shown for EUR-44 [EUR-11] for mean annual P and CV, respectively.



974
 975 **Figure 6.** Climatological monthly means of P for observations and GCM-RCM combinations of (a)
 976 EUR-44 and (b) EUR-11 aggregated at Full scale.

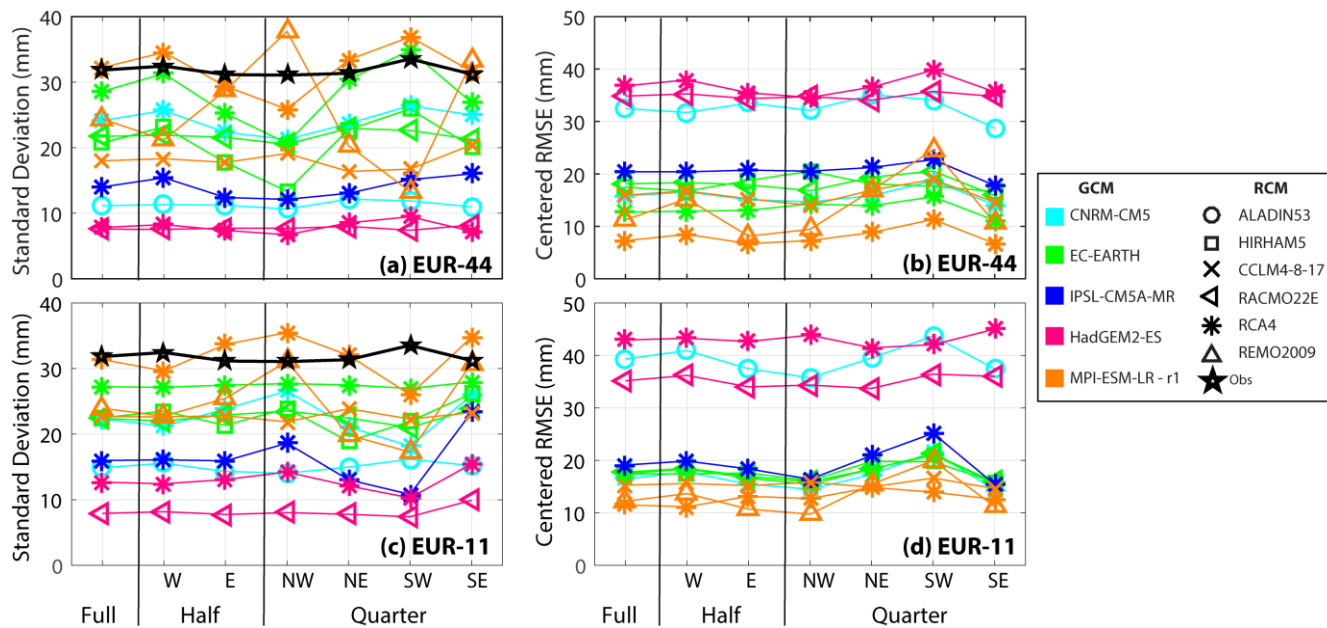
977
 978



979

980 **Figure 7.** Temporal Taylor diagram and seasonal bias computed for the GCM-RCM combinations of
 981 (a,b) EUR-44 and (c,d) EUR-11 aggregated at Full scale.

982

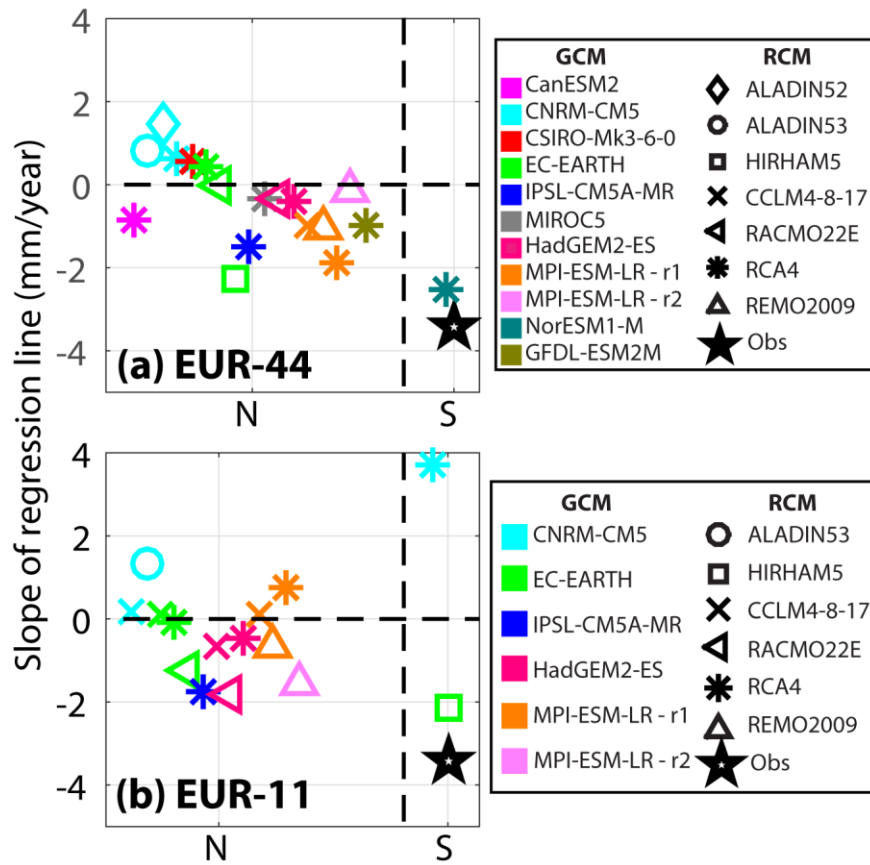


983

984

Figure 8. Standard deviation and centered RMSE between simulated and observed mean monthly P at different aggregation scales and locations for the GCM-RCM combinations available for both EUR-44 and EUR-11. In (a) and (b) [(c) and (d)], results are shown for EUR-44 [EUR-11] for CC and RMSE, respectively.

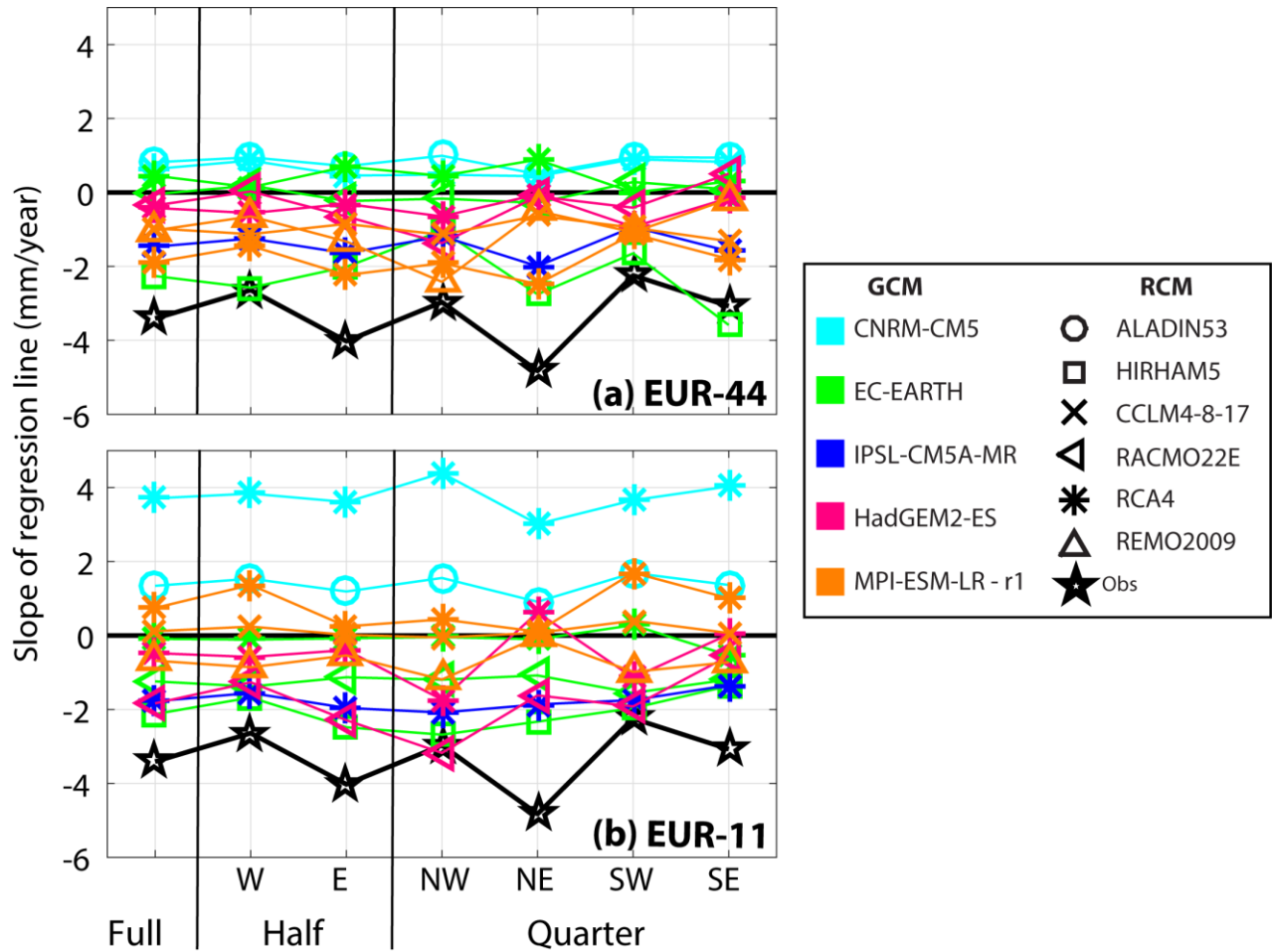
988



990

991 **Figure 9.** Slope of the linear trend for annual P observed and simulated at Full scale by the GCM-RCM
 992 combinations of (a) EUR-44 and (b) EUR-11. In each panel, the cases with significant (S) and non-
 993 significant (N) trends at 5% significance level are plotted to the left and right of the dashed line,
 994 respectively.

995

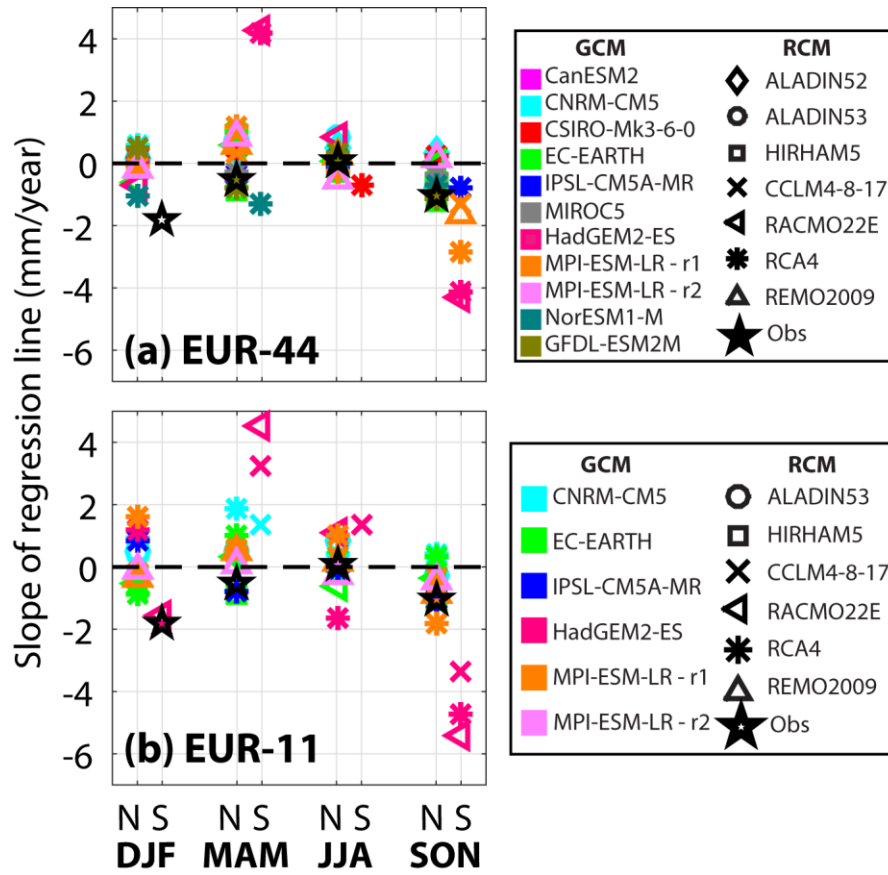


996

997 **Figure 10.** Slope of the linear trend for annual P observed and simulated at different aggregation scales
 998 and locations for the GCM-RCM combinations available for both (a) EUR-44 and (b) EUR-11. The
 999 observed trend is statistically significant in all cases. The simulated trends are never statistically
 1000 significant except the following cases. For EUR-44: EC-EARTH–HIRHAM at Quarter scale in NE.
 1001 For EUR-11: EC-EARTH–HIRHAM at Full scale, Half scale in W and Quarter scale in SE;
 1002 HadGEM2-ES–RACMO22E at Half scale in W and Quarter scale in SE; and CNRM-CM5–RCA4 at
 1003 Full scale, Half scale in E, and Quarter scale in NW.

1004

1005



1006

1007

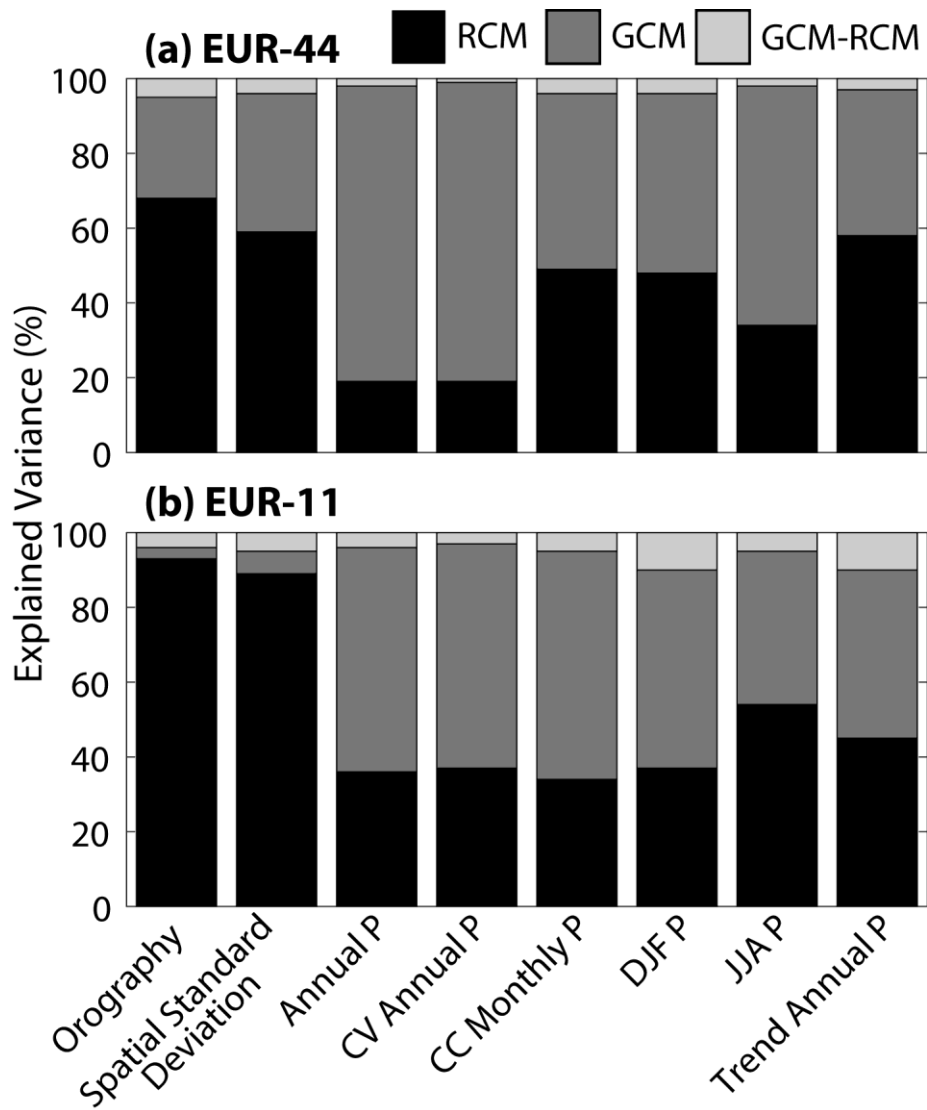
1008

1009

1010

1011

Figure 11. Slope of the linear trend for the mean seasonal P observed and simulated at Full scale by the GCM-RCM combinations of (a) EUR-44 and (b) EUR-11. In each panel, the cases with significant (S) and non-significant (N) trends at 5% significance level are plotted to the left and right of each season, respectively.

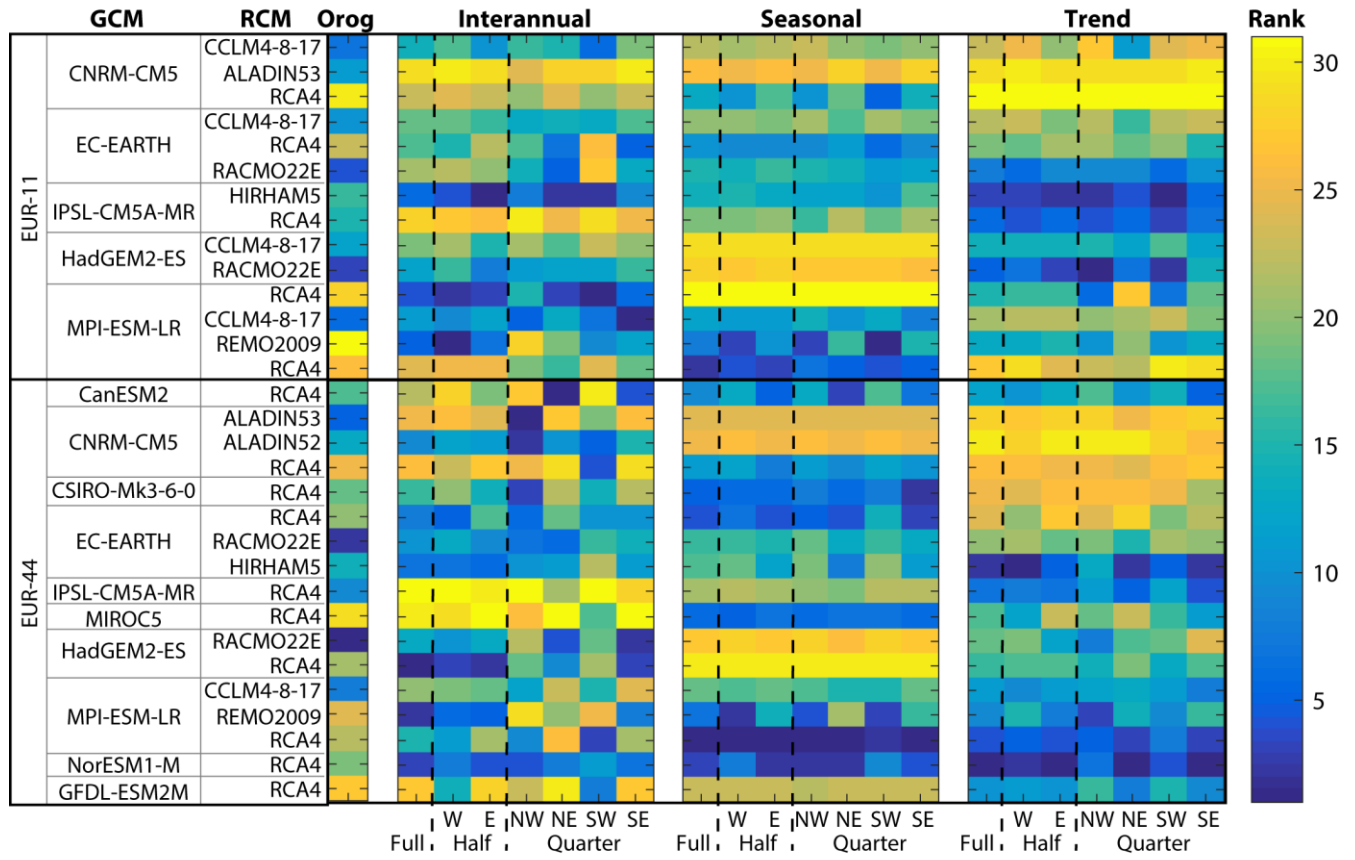


1012

1013 **Figure 12.** Percent of variance explained by RCM, GCM, and interaction between them (GCM-RCM)

1014 for a number of simulated variable (see main text for details).

1015



1016

1017 **Figure 13.** Ranks of the relative error ε_j defined in equation (6) and Table 5 for four P properties.

1018 “Orog” is the orographic effect on P (see Table 5 for the variables considered in error computation of
 1019 each property).

1020

1021 **Table Captions**

1022

1023 **Table 1.** Summary statistics of elevation and annual and seasonal mean P recorded by the rain gauges
1024 of the Sardinian Hydrologic Survey in the period 1950-2005. For each variable, the mean, standard
1025 deviation, minimum and maximum values across the gauges are reported. Seasons are defined as
1026 follows: DJF is December, January and February; MAM is March, April and May; JJA is June, July
1027 and August; and SON is September, October, and November.

1028

1029 **Table 2.** General Circulation Models (GCMs) used to drive the Regional Climate Models (RCMs) in
1030 the EURO-CORDEX Historical experiment at EUR-44 and EUR-11 resolutions for the GCM-RCM
1031 combinations used in this study (see Table 4).

1032

1033 **Table 3.** Regional Climate Models (RCMs) of the EURO-CORDEX Historical experiment at EUR-44
1034 and EUR-11 resolutions used in this study.

1035

1036 **Table 4.** GCM-RCM combinations of the EURO-CORDEX Historical experiment at EUR-44 and
1037 EUR-11 resolutions used in this study. For the MPI-ESM-LR GCM, two ensemble members are
1038 available with REMO2009. Framed entries highlight GCM-RCM combinations with both EUR-11 and
1039 EUR-44 runs that are compared in the analyses of the sensitivity to RCM grid resolution.

1040

1041 **Table 5.** Variables used to compute the dimensionless metric ε_j of equation (6) for different P
1042 properties and formula adopted to calculate the corresponding error. In the symbols used to indicate
1043 each variable, the subscripts “*obs*” and “*j*” refer to the values that were observed and simulated by the
1044 *j*-th GCM-RCM combination, respectively.

1045

Variable	Mean	Standard Deviation	Minimum	Maximum
Elevation (m asl)	326	297	0	1467
Annual P (mm)	710	168	316	1281
DJF P(mm)	261	72	69	495
MAM P(mm)	172	45	75	341
JJA P(mm)	43	17	9	202
SON P(mm)	228	52	102	454

1046

1047 **Table 1.** Summary statistics of elevation and annual and seasonal mean P recorded by the rain gauges
1048 of the Sardinian Hydrologic Survey in the period 1950-2005. For each variable, the mean, standard
1049 deviation, minimum and maximum values across the gauges are reported. Seasons are defined as
1050 follows: DJF is December, January and February; MAM is March, April and May; JJA is June, July
1051 and August; and SON is September, October, and November.

1052

Model	Short Name	Institution	Reference
CCCma CanESM2	CanESM2	Canadian Centre for Climate Modelling and Analysis	Arora et al. (2011)
CNRM CERFACS CNRM-CM5	CNRM-CM5	Centre National de Recherches Météorologiques, France	Voltaire et al. (2013)
CSIRO QCCCE Mk3.6.0	CSIRO-Mk3.6.0	Commonwealth Scientific and Industrial Research Organisation, Australia	Jeffrey et al. (2013)
EC-EARTH v2	EC-EARTH	EC-Earth Consortium, Europe	Hazeleger et al. (2012)
IPSL IPSL-CM5A-MR	IPSL-CM5A	Institut Pierre-Simon Laplace, France	Hourdin et al. (2013)
MIROC MIROC v5	MIROC5	University of Tokyo, Japan	Watanabe et al. (2010)
MOHC HadGEM2-ES	HadGEM2-ES	Hadley Met Office Hadley Centre, UK	Collins et al. (2011)
MPI MPI-ESM-LR	MPI-ESM-LR	Max Planck Institute for Meteorology (MPI-M)	Giorgetta et al. (2013)
NCC NorESM1-M	NorESM1-M	Norwegian Climate Centre	Bentsen et al. (2013)
NOAA-GFDL GFDL-ESM2M	GFDL-ESM2M	National Oceanic Atmospheric Administration - Geophysical Fluid Dynamics Laboratory, USA	Dunne et al. (2012)

1053

1054

Table 2. General Circulation Models (GCMs) used to drive the Regional Climate Models (RCMs) in

1055

the EURO-CORDEX Historical experiment at EUR-44 and EUR-11 resolutions for the GCM-RCM

1056

combinations used in this study (see Table 4).

1057

Model	Short Name	Institution	Reference
CLMcom CCLM4-8-17	CCLM4-8-17	Climate Limited-Area Modelling Community (www.clim- community.eu)	Baldauf et al. (2011); (Rockel et al., 2008)
CNRM ALADIN53	ALADIN53	Centre National de Recherches Météorologiques, France	Colin et al. (2010)
DMI HIRHAM5	HIRHAM5	Danmarks Meteorologiske Institut, Denmark	Bøssing Christensen et al. (2007)
HMS ALADIN52	ALADIN52	Hungarian Meteorological Service, Hungary	Colin et al. (2010)
KNMI RACMO22E	RACMO22E	Koninklijk Nederlands Meteorologisch Instituut, Netherlands	Van Meijgaard et al. (2008)
MPI-CSS REMO2009	REMO2009	Helmholtz-Zentrum Geesthacht, Climate Service Center, Max Planck Institute for Meteorology	Teichmann et al. (2013)
SMHI RCA4	RCA4	Sveriges Meteorologiska och Hydrologiska Institut, Sweden	Samuelsson et al. (2011)

1058

1059 **Table 3.** Regional Climate Models (RCMs) of the EURO-CORDEX Historical experiment at EUR-44
1060 and EUR-11 resolutions used in this study (see Table 4).

1061

	CCLM4-8-17	ALADIN53	HIRHAM5	ALADIN52	RACMO22E	REMO2009	RCA4
CanESM2	-	-	-	-	-	-	EUR-44
CNRM-CM5	EUR-11	EUR-44 EUR-11	-	EUR-44	-	-	EUR-44 EUR-11
CSIRO-Mk3.6.0	-	-	-	-	-	-	EUR-44
EC-EARTH	EUR-11	-	EUR-44 EUR-11	-	EUR-44 EUR-11	-	EUR-44 EUR-11
IPSL-CM5A	-	-	-	-	-	-	EUR-44 EUR-11
MIROC5	-	-	-	-	-	-	EUR-44
HadGEM2-ES	EUR-11	-	-	-	EUR-44 EUR-11	-	EUR-44 EUR-11
MPI-ESM-LR	EUR-44 EUR-11	-	-	-	-	EUR-44 (2) EUR-11 (2)	EUR-44 EUR-11
NorESM1-M	-	-	-	-	-	-	EUR-44
GFDL-ESM2M	-	-	-	-	-	-	EUR-44

1064 **Table 4.** GCM-RCM combinations of the EURO-CORDEX Historical experiment at EUR-44 and EUR-11 resolutions used in this study.

1065 For the MPI-ESM-LR GCM, two ensemble members are available with REMO2009. Framed entries highlight GCM-RCM combinations

1066 with both EUR-11 and EUR-44 runs that are compared in the analyses of the sensitivity to RCM resolution.

Property	Variable, k	Error, $E_{k,j}$
Orographic effect	Slope of the linear relation between mean annual P and elevation, SL	$ SL_{obs} - SL_j $
Interannual variability	Mean annual P, \bar{P}	$ \bar{P}_{obs} - \bar{P}_j $
	CV of annual P, CV	$ CV_{obs} - CV_j $
Seasonality	Monthly standard deviation, MSD	$ MSD_{obs} - MSD_j $
	Monthly correlation coefficient, CC	$1 - CC_j$
	Monthly root mean square error, $RMSE$	$RMSE_j$
Annual trend	Slope of the linear trend, SLT	$ SLT_{obs} - SLT_j $

1067

1068 **Table 5.** Variables used to compute the dimensionless metric ε_j of equation (6) for different P
1069 properties and formula adopted to calculate the corresponding error. In the symbols used to indicate
1070 each variable, the subscripts “*obs*” and “*j*” refer to the values that were observed and simulated by the
1071 *j*-th GCM-RCM combination, respectively.